

DNP-enhanced NMR of Lithium Dendrites: Selective Observation of the Solid–Electrolyte Interphase

Michael A. Hope,¹ Bernardine L. D. Rinkel,¹ Anna B. Gunnarsdóttir,¹ Katharina Märker,¹ Svetlana Menkin,¹ Subhradip Paul,² Ivan Sergeyev,³ Clare P. Grey¹

1. Department of Chemistry, University of Cambridge, Lensfield Road, Cambridge, CB2 1EW, U.K
2. School of Physics and Astronomy, University of Nottingham, University Park, Nottingham, NG7 2RD, U.K
3. Bruker Biospin Corp., 15 Fortune Drive, Billerica, MA, 01821, USA.

Abstract

Lithium metal anodes represent the ultimate target for batteries in terms of energy density but yet are plagued with low efficiencies and safety issues associated with dendrite formation. Critical to mitigating dendrite formation is an understanding of the solid–electrolyte interphase (SEI) layer which forms on anode surfaces such as lithium metal. NMR spectroscopy can provide important information on the SEI composition but suffers from issues of sensitivity and selectivity. Dynamic nuclear polarisation (DNP) boosts sensitivity in NMR by harnessing the greater polarisation of unpaired electrons; however, in typical exogenous DNP experiments a solution of organic radicals must be added, which are not selective for the SEI, require cooling the sample to cryogenic temperatures, and could react with the SEI/metal anode. Here we instead exploit the inherent conduction electrons to hyperpolarise the lithium metal at room temperature, utilising the Overhauser mechanism used in early pioneering DNP studies, but now with the benefit of much higher contemporary magnetic fields and microwave sources, resulting in enhancements of an order of magnitude for ⁷Li, as well as the enhancement of other nuclei. We selectively enhance the ⁷Li, ¹H and ¹⁹F NMR spectra of SEI species directly formed on the lithium metal microstructures, revealing the chemical nature and spatial distribution of organic and inorganic components, and exploring the effect of the fluoroethylene carbonate electrolyte additive. Our novel methodology paves the way for more ambitious *in-situ* DNP studies of batteries that can be performed at room temperature, and the selective enhancement of spins at the metal–diamagnetic solid interface has widespread implications for the study of many systems of interest to chemists and physicists.

Introduction

The development of longer lasting, higher energy density and cheaper rechargeable batteries represents one of the major technological challenges of our society.¹ Batteries are the limiting component in the shift from gasoline-powered to electric vehicles, and are also required to enable the increased use of typically intermittent renewable energy sources, to balance demand with generation.² One strategy to increase energy density involves the use of lithium metal in place of the commercial anode graphite, in a “lithium metal battery” (LMB).^{3,4} All-solid-state batteries (ASSBs), which replace the flammable organic liquid electrolyte of traditional lithium ion batteries (LIBs) with a safer solid alternative, will also require a lithium metal anode if they are to compete with LIBs in terms of energy density.⁵ Similarly, the high energies quoted for lithium air and sulphur batteries are generally based on the use of lithium metal anode.⁶ A commercially viable, room temperature, rechargeable battery with a lithium metal anode (LMB or ASSB) has yet to be developed, however, due to difficulties related to plating and stripping lithium and the low Coulombic efficiency upon cycling.^{1,3,7} Mossy and dendritic lithium structures form during plating, which can cause short circuits and severe safety concerns. Lithium deposits can also form on the graphite anode of a traditional LIB upon fast charging, particularly at low temperatures, again with serious potential safety issues.⁸

While lithium deposition at high rates is largely dictated by the mobility of ions in the electrolyte, Li

microstructures are still formed at low rates, in processes that are controlled by the nature of the passivating layer that grows on the lithium metal.^{4,9,10} This layer, the solid electrolyte interphase (SEI), is formed by degradation of the electrolyte on contact with strongly reducing lithium metal, resulting in a highly heterogeneous film, with inorganic species typically found closer to the metal surface and organic species closer to the bulk electrolyte.¹¹ Non-uniform Li⁺ transport across the SEI film creates instabilities and nucleation points which determine the extent and nature of the lithium microstructure formation.^{12,13}

An extensive range of analytical techniques has been applied to study the nature of the SEI, including X-ray photoelectron spectroscopy (XPS)^{14,15} and time-of-flight secondary-ion mass spectrometry (TOF-SIMS)¹⁶, however the nature and distribution of chemical components in the SEI, the Li⁺ mobility within them, and their relationship to dendrite formation, are still relatively unclear. Significant strides have also been made to study the SEI with NMR spectroscopy,^{17,18} however NMR can suffer from issues of sensitivity and selectivity.

Dynamic nuclear polarisation (DNP) is a promising approach to address sensitivity issues, and the method has exploded over the last few years due to developments in high power microwave sources at the higher frequencies needed for high resolution NMR.^{19–21} DNP exploits the ~10³ times greater gyromagnetic ratio of paramagnetic electrons to hyperpolarise the nuclear spins and hence increase the signal in NMR experiments, by irradiating the electron spin resonance (ESR) transitions with microwaves.²⁰ To date, the SEI on reduced graphene oxide and silicon anodes has been studied by exogenous DNP,^{22–24} whereby a solution of organic radicals is added to the system which is then cooled to cryogenic temperatures (100 K or below) to slow the electron relaxation times (T_{1e}) of the radicals so that the ESR transition can be more easily saturated.^{20,25} This approach has several limitations: (i) the addition of an organic radical solution may alter the nature of SEI such that the results from such experiments may not be representative; (ii) the organic radicals are not stable over the large voltage window that most batteries operate in; (iii) the organic radicals are external to the SEI so cannot be readily used to probe the SEI–metal interface; (iv) exogenous DNP is not selective to the SEI and can also enhance any impurities in the system, which could then be mistaken for components of the SEI; and (v) since the experiments are performed at 100 K they cannot be coupled with *in-situ* electrochemical cycling or used to study Li⁺ dynamics. Endogenous DNP has been used to investigate bulk battery anodes doped with paramagnetic metal ions,²⁶ but this is not immediately applicable to the study of interfacial structures.

Intriguingly, the first DNP experiments were performed on lithium metal more than 60 years ago *at room temperature*²⁷ and yet this approach is no longer used. Here, instead of localised radicals, the Pauli paramagnetism of the metallic electrons is exploited to enhance nuclear magnetization via the Overhauser effect:²⁸ on irradiation of the conduction ESR (CESR) transition, cross relaxation of the electrons induces hyperpolarisation of the ⁷Li nuclei. Furthermore, although the T_{1e} of lithium metal is short (~10 ns, depending on the purity,²⁹ c.f. >10 μs for commonly used organic radicals at 100 K²⁰), the relaxation is dominated by impurities in the metal and is largely temperature independent;²⁹ this removes the need to cool samples to cryogenic temperatures, potentially allowing higher temperature phenomena to be studied. We therefore asked the following questions: could room temperature Li-metal DNP be achieved with modern higher field magnets and the much higher power microwave sources now available? And could the saturation of the electron spins be used to polarize nearby diamagnetic nuclei? LMBs are well-suited for this study because the microstructural morphology formed on lithium plating exposes a large surface area of lithium metal to interact with microwave irradiation and to form the SEI.

This paper reports the significant hyperpolarisation of the room temperature ⁷Li NMR signal of cycled lithium metal anodes under magic angle spinning (MAS), and confirms the Overhauser mechanism as the source of the enhancement. The hyperpolarisation is then harnessed to selectively enhance the

diamagnetic components of the SEI observed in the ^7Li , ^1H and ^{19}F NMR spectra; this allows the SEI to be distinguished without rinsing the electrodes to remove the excess electrolyte and salts that can obscure conventional NMR spectra, a process which may lead to the partial dissolution of the SEI and changes in structure and composition.³⁰ The DNP enhancements allow the proximity of different species in the SEI to the metal surface to be inferred, while double resonance experiments such as $^7\text{Li} \rightarrow ^1\text{H}$ cross polarisation (CP), $^7\text{Li} \rightarrow ^{19}\text{F}$ CP, and $^7\text{Li}\{\text{ }^{19}\text{F}\}$ rotational echo double resonance (REDOR³¹) are further used to identify minor components such as polymeric organic species and LiF. The chemical composition and structure of the SEI layer is highly dependent on the electrolyte system used, so we compare samples prepared from electrolytes with and without the common additive fluoroethylene carbonate (FEC), which has been shown to yield a more uniform lithium deposition and improved electrochemical performance.³²⁻³⁷ Finally, a comparison is made with experiments on static samples to evaluate the feasibility of *in-situ* experiments on working batteries.

Methods

As described in more detail in the Supplementary Information (with a full list of samples A – G given in Table S1), lithium metal was deposited onto either lithium disks (samples A, D – G) or copper disks (samples B, C) in coin cells with 75 μL of either 1 M LiPF₆ in ethylene carbonate/dimethyl carbonate 1:1 vol (EC:DMC; Sigma Aldrich, battery grade), referred to as LP30 (samples B, C, D, F), or the same electrolyte with 10% vol of FEC (Sigma Aldrich, anhydrous), referred to as LP30+FEC (samples A, E, G). After galvanostatic electrodeposition with current densities ranging from 0.033 to 1.25 mA cm⁻², the coin cells were disassembled in an Ar atmosphere glovebox and the microstructures scraped off gently with a razorblade without rinsing. The sample was then diluted by $\sim 5\times$ by mass with KBr (previously dried at 200 °C for 24 hours) to improve microwave penetration and allow the metallic samples to be more easily spun, before packing into a 3.2 mm outer (2.2 mm inner) diameter sapphire rotor.

The majority of the DNP NMR experiments were performed at the UK DNP MAS NMR Facility at the University of Nottingham, UK on a 14.1 T AVANCE III HD spectrometer with a 395 GHz gyrotron microwave source. Additional experiments were performed at Bruker Billerica, USA on a 9.4 T AVANCE NEO spectrometer with a 263.7 GHz gyrotron or a 264.6 GHz klystron. In both cases, a 3.2 mm wide bore probe was used. Details of the NMR experiments are given in the figure captions and the Supplementary Information.

Results and Discussion

Lithium Metal DNP

Figure 1a shows the room temperature (14.1 T) ^7Li MAS NMR spectrum of microstructural lithium (sample A), with and without 16.5 W of microwave irradiation. The large shift of the Li metal signal (>200 ppm) is due to the Fermi contact interaction with the Pauli paramagnetic moment of the conduction electrons, a so-called Knight shift.³⁸ Two clear observations can be made: first, a noticeable enhancement of the lithium metal signal of 7.9 is seen based on the peak area ($\varepsilon_{\text{area}}$); second, microwave irradiation results in a spreading of the NMR signal to lower frequencies, so that the enhancement, based on the peak height is lower ($\varepsilon_{\text{peak}} = 4.9$). The latter is ascribed to partial saturation of the CESR transition which reduces the moment and hence the Knight shift; the greater the microwave power, the greater the saturation and the lower the observed shift (Figure S1). Early experiments also demonstrated this effect at 0.34 T, where the Knight shift was reduced by $\sim 75\%$ due to the much greater saturation of the CESR transition at the lower field.³⁹ The distribution of frequencies for the resonance is tentatively ascribed to differences in the degree of CESR saturation in the sample resulting from inhomogeneities of both the sample and the microwave field.

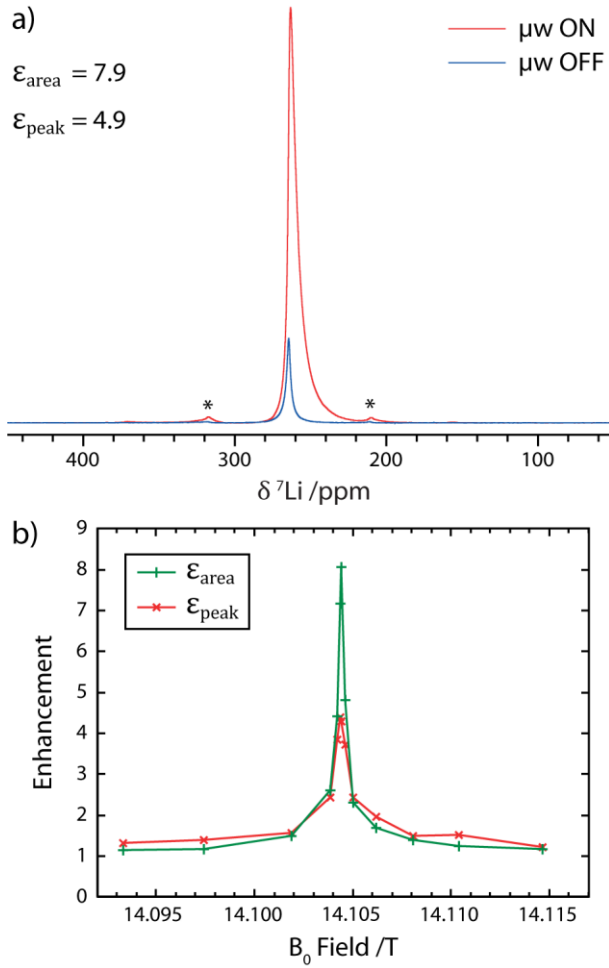


Figure 1: a) ${}^7\text{Li}$ NMR spectrum of microstructural lithium metal (sample A), with and without 15.6 W of microwave irradiation at 395.29 GHz ($\mu\text{w ON/OFF}$), recorded at 14.1045 T, 12.5 kHz MAS and a sample temperature of ~ 300 K, using a Hahn echo pulse sequence, a recycle delay of 0.25 s and 80 scans. Spinning sidebands are marked with an asterisk. b) The enhancement of the integrated intensity and peak intensity as a function of the B_0 field (sample B), measured at 100 K.

To determine the effect of temperature on the DNP enhancement, the experiment was repeated at 100 K, yielding an enhancement of $\varepsilon_{\text{area}} = 7.3$ (Figure S2), i.e. of comparable magnitude. A field sweep performed on a second sample (B) confirms the DNP mechanism (Figure 1b); a single, sharply peaked positive enhancement is observed at the Li CESR frequency, indicating an Overhauser mechanism for which zero-quantum cross-relaxation dominates, given that the gyromagnetic ratio of ${}^7\text{Li}$ is positive.²⁰ The electron g-factor corresponding to the peak enhancement is 2.0024 ± 0.0002 , compared to 2.0026 from the peak absorbance in the X band ESR spectrum (Figure S3). A narrower sweep at room temperature for sample A reveals the same sharp feature (Figure S4), at the same field, as expected since the position of the CESR resonance is temperature independent (Figure S3). The field at which the optimal enhancement is achieved depends slightly on the applied microwave power (Figure S5 and Figure S6), which is also observed for the peak absorbance of the ESR spectrum (Figure S8 and Figure S9) and may be due to partial saturation effects.⁴⁰ There is no evidence of a solid effect, which would occur at magnetic fields of ± 8.3 mT from the CESR resonance.

Further experiments performed at a lower field strength of 9.4 T with 44 W of gyrotron irradiation on a third sample (C) yielded higher enhancements of $\varepsilon_{\text{area}} = 18$ at room temperature and $\varepsilon_{\text{area}} = 27$ at 100 K (Figure S10), the higher enhancements being ascribed to a combination of the higher microwave power achievable, the lower field, and variations between samples. Moreover, even with a lower power klystron source (~ 2.7 W), enhancements could be achieved at this field on this sample of $\varepsilon_{\text{area}} = 7.6$ at

room temperature and $\varepsilon_{\text{area}} = 11$ at 100 K (Figure S11), potentially further reducing the technological requirements and cost of running these experiments.

The temperature dependence of the enhancement appears to depend on a number of factors including the magnetic field (see Figure S7), and sample dependent factors such as the morphology, and the T_1 and T_{1e} relaxation constants, which will both be affected by the presence of paramagnetic impurities. For example, the greater enhancement sometimes seen at lower temperatures is at least in part due to differences in the ${}^7\text{Li}$ spin lattice relaxation times (T_1) of the metal, which was measured as 0.36 s at 100 K compared to 0.14 s at room temperature (sample G, Table S4). These phenomena are currently under further investigation, but similar enhancements are nevertheless achieved between 100 K and room temperature.

The Metal–SEI Interface

Having demonstrated Overhauser DNP enhancement of the lithium metal signal at high magnetic fields, experiments were then performed to determine if this hyperpolarisation can be exploited to probe the interface between the SEI and lithium metal. Two representative samples were chosen, one prepared with a standard electrolyte LP30, and the second with 10 vol% of the additive FEC (samples D and E, Figure 2). Two further samples prepared in the same way corroborate the results (samples F and G, Figure S13). The metallic ${}^7\text{Li}$ signal is again enhanced for all samples (Figure S12), although there is a spread of enhancements ($\varepsilon_{\text{area}} = 6 – 13$) which does not correlate with the electrolyte used and is ascribed to factors such as variations in the T_{1e} and the surface-to-volume ratio. Importantly, there is still sufficient hyperpolarisation in all cases to investigate the SEI.

Firstly, microwave irradiation of the Li CESR resonance produces clear enhancements in the ${}^7\text{Li}$ diamagnetic signals from the SEI that surprisingly are of the same order as that seen for the metal itself (Figure 2a–d, Table 1); these must correspond to lithium species within the SEI. The broad resonance at 0.7 ppm can be attributed to salts such as Li_2CO_3 at 0 ppm^{41,42} and LiOH at 1 ppm,⁴³ whereas the minor component at –0.3 ppm could arise from CH_3OLi or residual electrolyte trapped in the SEI layer^{30,43}. The sharp component in the LP30 spectrum at –0.8 ppm is not enhanced and is therefore ascribed to Li^+ in the residual electrolyte, as the electrodes were not rinsed after disassembly.

The sample formed with the LP30+ FEC electrolyte also exhibits a signal at –0.9 ppm, but it is broader than for the LP30 sample and is enhanced by microwave irradiation (Figure 2c,d). This suggests that there is residual electrolyte closer to the metal surface, perhaps due to a thinner SEI, or that there is more effective spin diffusion through the SEI due to a greater density of ${}^7\text{Li}$ spins. A minor signal is seen at –0.8 ppm with a large enhancement of 10.3, indicating that the corresponding species is close to the lithium metal surface; on the basis of the shift it is tentatively assigned to LiF arising from reduction of FEC^{36,37} and the decomposition of the LiPF_6 salt^{44,45}. There is again a broad enhanced signal, now centred at 0.1 ppm, corresponding to the lithium carbonate and hydroxide species in the SEI.

Irradiation of the CESR transition is also found to enhance the signal of other nearby nuclei, via mechanisms that will be discussed below. This allows the organic compounds that form a key part of the SEI to be identified. ${}^1\text{H}$ NMR spectra (Figure 2e,g; deconvolutions in Table S5, Figure S17 and Figure S18) were recorded with and without microwave irradiation at 240 K, because room temperature is close to the melting point of ethylene carbonate (~310 K) and it is challenging to maintain a constant temperature between the microwave on and off experiments. Although the enhancements are not large, the intensity clearly increases on application of microwaves; furthermore, the spectra are not enhanced uniformly, so the signals arising from the SEI can be distinguished from the significant background intensity.

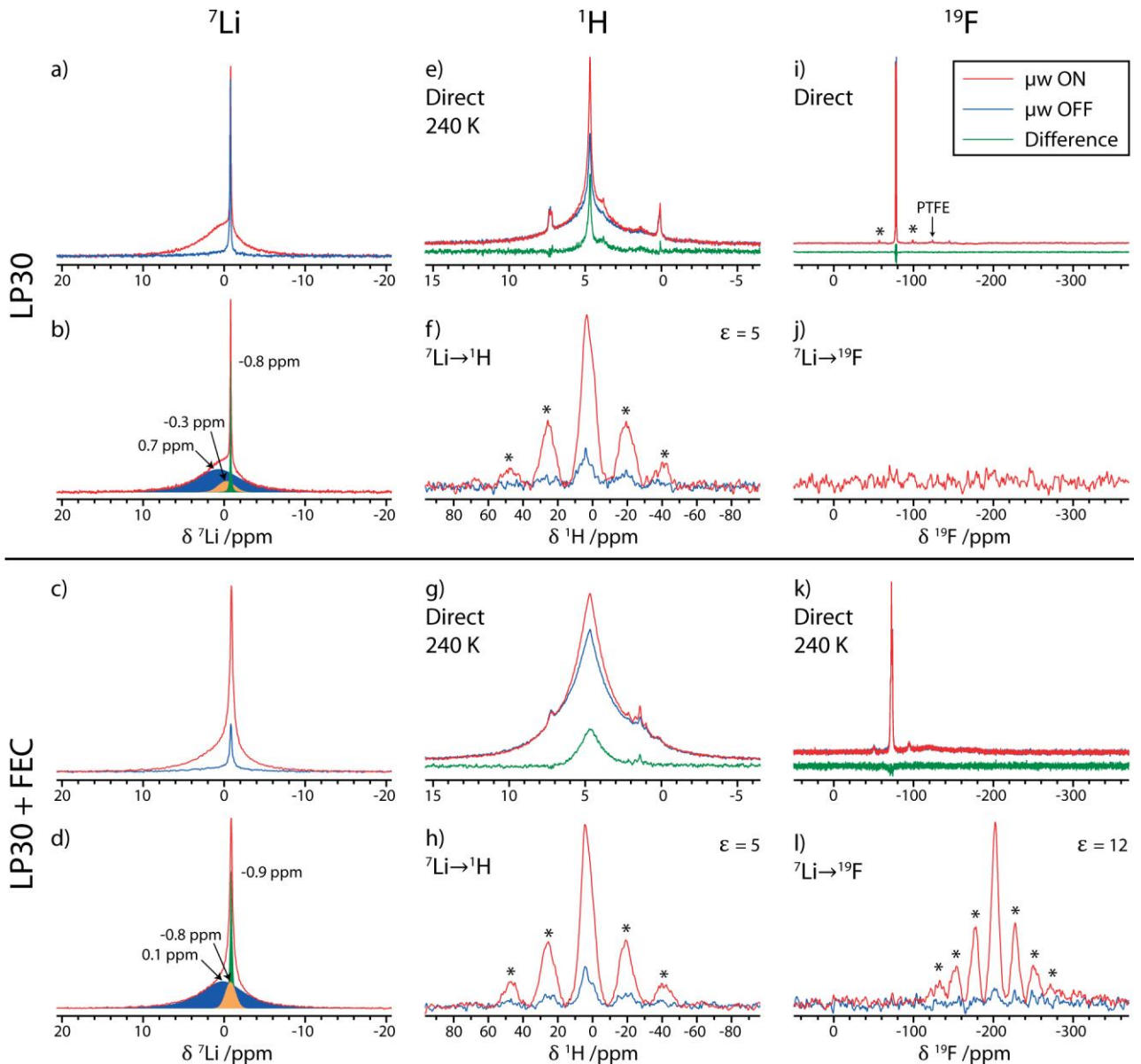


Figure 2: Diamagnetic ^7Li (a–d), ^1H (e–h), and ^{19}F (i–l) NMR spectra of lithium microstructures produced by cycling with the LP30 (top half, sample D) and LP30+FEC (bottom half, sample E) electrolytes, recorded with and without 15.6 W of microwave irradiation ($\mu\text{w ON/OFF}$). b) and d) are deconvolutions of the $\mu\text{w ON}$ spectra in a) and c), respectively. All spectra were recorded at 12.5 kHz MAS, 14.1 T and room temperature, unless otherwise stated. Spinning sidebands are marked with asterisks. The direct spectra were recorded with a Hahn echo pulse sequence and the CP spectra were recorded with the ^7Li carrier at 0 ppm and contact times of 1 ms and 0.1 ms for $^7\text{Li}\rightarrow^1\text{H}$ and $^7\text{Li}\rightarrow^{19}\text{F}$ respectively. For the direct ^1H and ^{19}F experiments, the difference between the spectra recorded with and without microwave irradiation is also shown. Recycle delays and experimental times are given in Table S2.

Table 1: Deconvolution and DNP enhancements (ϵ) of the ${}^7\text{Li}$ signals (Figure 2a–d and Figure S12) of microstructural lithium deposited from the LP30 and LP30+FEC electrolytes. See Figure S14 and Figure S15.

LP30				
Chemical shift /ppm	-0.8	-0.3	0.7	264
FWHM /ppm ^a	0.1	2.4	6.6	—
Integration ^b	11%	11%	78%	—
ϵ	0.95	4.8	8.1	13
LP30 + FEC				
Chemical shift /ppm	-0.9	-0.8	0.1	264
FWHM /ppm ^a	0.3	1.5	6.4	—
Integration ^b	22%	13%	65%	—
ϵ	3.9	10.3	5.6	6.2

^aFull-width at half-maximum

^bRelative integrated intensity of the diamagnetic signals in the microwave on spectra.

For the LP30 sample, the greatest enhancement is for the 3.8 ppm signal, which can only be seen with microwave irradiation, and is assigned to poly-ethylene oxide (PEO)-like species formed through the decomposition of EC molecules; these have been shown to be the major species present in the SEI formed on silicon anodes.^{23,30} Additionally, there are two sharp resonances at 4.68 and 4.74 ppm, which exhibit comparably large enhancements of ~2. These are ascribed to more mobile EC molecules trapped within pores in the SEI, and/or small organic lithium carbonates such as lithium ethylene dicarbonate (LEDC), which are sufficiently close to the metal surface to be enhanced. The same sharp signals are not observed for the LP30+FEC sample, which suggests that the SEI is less porous to the electrolyte and/or that these organics are further from the Li metal in this case.

For the LP30+FEC sample, a noticeably broader signal at ~4.7 ppm is observed with an enhancement of 1.8, from more rigid organic polymers in the SEI such as poly-vinylene carbonate (poly-VC), produced by cross-linking of the degradation species; notably, no PEO signal is seen. This is consistent with the products formed from chemically reduced FEC,³⁶ and again with the SEI seen on silicon anodes, where the addition of FEC was shown to result in more cross-linking.^{23,24} The other signals at around 1 – 2 ppm, seen in both samples with minor enhancements, are ascribed to aliphatic groups, such as in lithium butylene dicarbonate (LBDC)-like species, which form from the reaction of more than one EC/FEC molecule at low potentials.³⁰ For both samples, the broad resonance at 4.5 – 4.7 ppm that is not enhanced is assigned to solid residual EC electrolyte, broadened by significant homonuclear dipolar coupling. The unenhanced signals at 0.1–0.2 and 7.2–7.3 are ascribed to impurities (most likely grease and an ammonium salt, respectively).

To improve the sensitivity of the ${}^1\text{H}$ spectra, ${}^7\text{Li} \rightarrow {}^1\text{H}$ CP experiments were performed which exploit the greater enhancement of the ${}^7\text{Li}$. The room temperature ${}^7\text{Li} \rightarrow {}^1\text{H}$ CP spectra (Figure 2f,h) exhibit broad asymmetric signals for both samples with full-widths at half-maximum of ~8.5 ppm, which are ascribed to polymeric species and organic carbonates coordinated to or nearby lithium ions;^{23,30} these broad signals are obscured in the direct ${}^1\text{H}$ spectra. The signal for the LP30 sample has a centre of mass of 2.5 ppm, whereas for the LP30+FEC sample the centre of mass is at a higher shift of 3.0 ppm; this is consistent with the greater proportion of poly-VC species in the latter due to FEC decomposition. Both samples exhibit noticeable enhancements of around $\epsilon = 5$, which is similar to the enhancements of the diamagnetic ${}^7\text{Li}$, and the species could also be reproducibly identified in the second set of samples (Figure S13f,h). The CP predominantly occurs from the diamagnetic lithium rather than the lithium metal nuclei, as demonstrated by performing experiments with ${}^7\text{Li}$ carrier frequencies corresponding to either the metal or diamagnetic ${}^7\text{Li}$ signals (Figure S16).

¹⁹F NMR spectra were acquired to improve our assignments of the species found at the metal–lithium interface. Only the signal from the PF₆⁻ anion at -72 ppm can be observed in the direct ¹⁹F spectra for both samples (Figure 2i,k); furthermore, this resonance is not enhanced upon microwave irradiation, indicating that the species is not close to the lithium metal, which supports the current understanding that the SEI is impermeable to PF₆⁻.¹¹ For the FEC sample, there are two signals at around -72 ppm (enlarged in Figure S19), which are ascribed to PF₆⁻ species in different coordination environments; no signal from residual FEC is seen, presumably due to it having evaporated. While no LiF signal at -203 ppm could be observed in the direct ¹⁹F NMR spectra for either sample, a clear signal was observed in the ⁷Li→¹⁹F CP spectrum for the LP30+FEC sample (Figure 2l) with a large enhancement of $\varepsilon \approx 12$. This is more than double the enhancement of the broad diamagnetic ⁷Li signal, which implies that LiF in the SEI is closer to the surface than other lithium species on average. Again, the CP occurs predominantly from the diamagnetic lithium, rather than from the metal surface, as shown by varying the ⁷Li carrier frequency (Figure S20); however, the enhancement still demonstrates proximity to the metal, since only diamagnetic lithium near the metal surface can be hyperpolarised. The presence of LiF for the LP30+FEC sample is also supported by ⁷Li{¹⁹F} REDOR experiments, which exhibit dephasing on ¹⁹F recoupling (Figure S21), although only of a minor component of the signal. There is a significant enhancement of the difference spectrum, $\varepsilon_{area} = 8$ (Figure S22) providing further evidence that LiF in the SEI is close to the metal surface. No LiF is seen for the LP30 sample (D) in the ⁷Li→¹⁹F CP or ⁷Li{¹⁹F} REDOR experiments (Figure 2j and Figure S24), which is consistent with its formation from FEC reduction. For the second LP30 sample (F), an extremely weak LiF signal was observed in the ⁷Li→¹⁹F CP spectrum (Figure S13j), but again significantly more LiF is present for the second LP30+FEC sample (G, Figure S13l).

Mechanisms and Spatial Considerations of Metal and SEI Hyperpolarisation

To explore the selectivity of lithium metal DNP to the metal–SEI interface, first the spatial dependence of the lithium metal enhancement should be considered, which depends on a number of factors. As lithium metal is a conductor, electromagnetic radiation is limited to the skin depth,⁴⁶ for microwave irradiation at 395 GHz, the skin depth is ~0.2 μm (see Supplementary Information). This would suggest that electrons are only saturated at the surface, in theory limiting the extent of enhancement. However, the paramagnetic electrons near the Fermi level also diffuse rapidly with kinetic energies corresponding to the Fermi energy. An electron retains its saturation on average for a time T_{2e} , during which it diffuses a distance known as the spin depth, given by $\sqrt{2DT_{2e}}$,⁴⁷ for lithium metal at room temperature, using the T_{1e} extracted from the power saturation of $\sim 6 \times 10^{-8}$ s (assuming $T_{1e} = T_{2e}$) and the electron diffusivity $D = 21 \text{ cm}^2 \text{ s}^{-1}$,⁴⁸ this yields a spin depth of ~16 μm. Comparing this to the average diameter of the lithium dendrites, ~0.5 μm (see Figure S25 and Figure S26), the electron saturation and hence lithium hyperpolarisation are expected to be uniform within the dendrites. The radiofrequency pulses used to record the ⁷Li NMR spectrum at 233 MHz have a skin depth of ~8 μm, so the microstructural lithium metal is uniformly observed.

Although the hyperpolarisation of the lithium metal is not surface selective on the length-scale of microstructural lithium, the enhancement of the metal–SEI interface is still selective since only the SEI, which is in contact with the metal, will be enhanced. Hyperpolarisation of diamagnetic ⁷Li in the SEI can occur either directly via the Overhauser DNP mechanism, if the nuclei are sufficiently close to interact with the conduction electrons, or via spin diffusion from the hyperpolarised ⁷Li metal. For both mechanisms, polarisation then propagates away from the metal surface through the diamagnetic ⁷Li nuclei in the SEI by spin diffusion and the selectivity to the SEI–metal interface is therefore determined by the spin diffusion rate and the DNP build-up time used.

For the direct ¹H experiments, there are also two possible mechanisms via which the hyperpolarisation could occur. If there are ¹H nuclei close to the metal surface, they could be hyperpolarised directly via

the Overhauser DNP effect, and this hyperpolarisation could propagate through spin diffusion if there is a sufficient density of ^1H spins. Alternatively, hyperpolarisation could, in principle, be induced by cross-relaxation with hyperpolarised diamagnetic ^7Li via a nuclear Overhauser effect; experiments to test this proposal are underway. In either case, species closer to the metal surface (i.e. in the SEI) will experience a greater enhancement. The comparatively low direct ^1H enhancements could be due to a low density of ^1H nuclei in the immediate proximity of the metal surface, as this region is expected to be more inorganic-rich, and/or due to a relatively inefficient hyperpolarisation mechanism.

Static Lithium Metal DNP

Finally, although MAS experiments offer the best chemical resolution, it is extremely challenging to perform *in-situ* electrochemical experiments under spinning conditions, and such experiments are necessary to study dynamic processes such as SEI formation and degradation in battery systems, as well as to detect transient species.⁴⁹ An *in-situ* MAS cell has recently been demonstrated,⁵⁰ but extremely slow cycling was necessary and metal electrodes were not used. To test whether the methodologies presented here could be applicable to *in-situ* studies, ^7Li NMR spectra were recorded under static conditions at 9.4 T, with and without microwave irradiation (Figure 3). The resonances are broader, but an appreciable enhancement of the metallic signal is still observed ($\varepsilon_{area} = 13$, c.f. $\varepsilon_{area} = 18$ under MAS, Figure S10a), as well as minor enhancement of the diamagnetic signal, particularly of the sharper component. Experiments to harness this enhanced polarisation to investigate other nuclei are in progress.

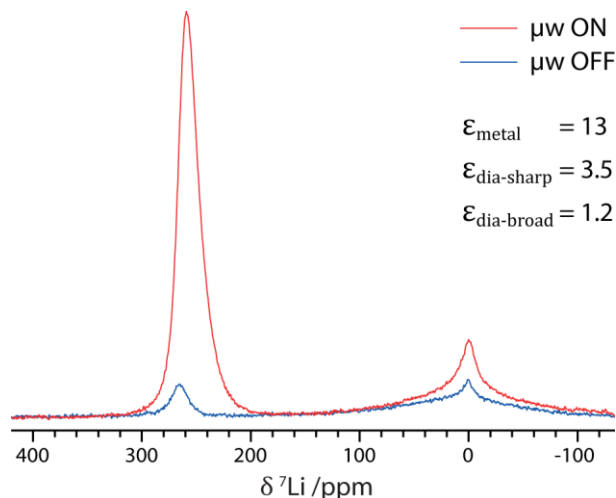


Figure 3: Static ^7Li NMR spectrum of microstructural lithium (sample C), recorded with and without microwave irradiation at 263.7 GHz and 44 W, at 9.4 T and room temperature, using a Hahn echo pulse sequence, a 0.25 s recycle delay and 128 scans. Shown too are the enhancements by area of the different signals.

Conclusions

High-field room temperature Overhauser DNP of lithium metal has been demonstrated for samples of electrodeposited microstructural lithium metal, with enhancements of around an order of magnitude. The polarisation source is intrinsic to the system, the addition of potentially reactive radicals is not required, and hyperpolarisation is selectively achieved for the species of interest. The enhancement can also be increased at lower field and with higher microwave powers. Notably, by removing the need for cryogenic temperatures, the technological requirement for performing such DNP experiments is significantly reduced.

The hyperpolarisation of the lithium metal has further been harnessed to selectively investigate the SEI via the ^7Li , ^1H and ^{19}F NMR spectra, specifically in this case to determine the effect of the FEC electrolyte additive. Selective enhancement of the ^1H NMR spectra distinguishes the organic SEI components, showing that the addition of FEC to the electrolyte reduces the amount of trapped EC in the SEI and promotes the formation of poly-VC species at the expense of PEO-like species. The greater enhancement of the diamagnetic ^7Li nuclei can be harnessed to increase the polarisation of ^1H and ^{19}F nuclei via CP, which reveals polymeric species and LiF in the SEI, respectively. The latter has a significantly higher concentration with the addition of FEC. Furthermore, the greater enhancement of the LiF $^7\text{Li} \rightarrow ^{19}\text{F}$ CP signal relative to that of the overall diamagnetic ^7Li signal provides compelling evidence that this inorganic species is closer on average to the lithium metal surface than other Li-containing species in the SEI. While there are many factors that affect the composition of the SEI, selective observation of the SEI via Overhauser DNP as demonstrated here will help to identify the critical factors for the formation of a stable, uniform, SEI which can minimise lithium dendrite growth in LMBs and other battery systems.

In principle, the Overhauser mechanism can operate for any metallic material, and the study of metal anodes for next-generation Na, K and Mg batteries could also be envisaged, or even graphitic and LiCoO_2 electrodes, which are metallic for certain degrees of lithiation. The enhancement afforded by Overhauser DNP of lithium metal could also find application in investigating very small masses of lithium metal, such as the dendrites which can also form in commercial lithium-ion batteries due to heterogenous local current densities under fast-charging conditions,⁸ as well as in lithium-metal solid-state batteries;⁵ such dendrites are challenging to study due to their low mass, but are of great importance in preventing short-circuits. Other applications in solid state chemistry and physics to examine buried metallic–diamagnetic interfaces can be readily imagined.

Finally, although resolution is reduced, preliminary experiments show that appreciable ^7Li enhancements can still be achieved by Overhauser DNP under static conditions, which suggests that *in situ* experiments will be possible whereby DNP can be used to selectively observe the species of interest (e.g. dendritic lithium and/or the SEI), in a working (battery) system where the presence of other components such as the electrolyte would typically drown out such signals. This could allow for the study of SEI formation and growth, one of the fundamental open questions regarding the SEI.¹¹

Acknowledgements

MAH and ABG acknowledge support from the Royal Society (RP/R1/180147). MAH is also grateful to the Oppenheimer foundation and ABG acknowledges EPSRC-EP/M009521/1. BLDR was supported by NECCES, an Energy Frontier Research Centre funded by the U.S. Department of Energy, under Award No. DE-SC0012583. KM and CPG acknowledge funding from the ISCF Faraday Challenge Fast Start project on “Degradation of Battery Materials” made available through grant EP/S003053/1. SM thanks the Blavatnik Cambridge Fellowships. The Nottingham DNP MAS NMR Facility is funded by the University of Nottingham and EPSRC (EP/L022524/1). We would like to thank Remington Carey and Prof. H. Sirringhaus (University of Cambridge) for the acquisition of X-band EPR spectra of lithium metal; Prof. Lauren Marbella (Columbia University) for providing additional samples for experiments in the US; and Dr Melanie Rosay and Dr. Ralph Weber (Bruker Billerica, US) for helpful discussions, assistance setting up the experiments at 9.4 T and measuring the Li T_{1e} .

References

1. Goodenough, J. B., Abruna, H. D. & Buchanan, M. V. *Basic Research Needs for Electrical Energy Storage. Report of the Basic Energy Sciences Workshop on Electrical Energy Storage, April 2-4.* (2007).
2. Chu, S., Cui, Y. & Liu, N. The path towards sustainable energy. *Nat. Mater.* **16**, 16 (2016).
3. Wood, K. N., Noked, M. & Dasgupta, N. P. Lithium Metal Anodes: Toward an Improved Understanding of Coupled Morphological, Electrochemical, and Mechanical Behavior. *ACS Energy Lett.* **2**, 664–672 (2017).
4. Liu, B., Zhang, J.-G. & Xu, W. Advancing Lithium Metal Batteries. *Joule* **2**, 833–845 (2018).
5. Manthiram, A., Yu, X. & Wang, S. Lithium battery chemistries enabled by solid-state electrolytes. *Nat. Rev. Mater.* **2**, 16103 (2017).
6. Bruce, P. G., Hardwick, L. J. & Abraham, K. M. Lithium-air and lithium-sulfur batteries. *MRS Bull.* **36**, 506–512 (2011).
7. Fang, C., Wang, X. & Meng, Y. S. Key Issues Hindering a Practical Lithium-Metal Anode. *Trends Chem.* **1**, 152–158 (2019).
8. Waldmann, T., Hogg, B.-I. & Wohlfahrt-Mehrens, M. Li plating as unwanted side reaction in commercial Li-ion cells – A review. *J. Power Sources* **384**, 107–124 (2018).
9. Chang, H. J. *et al.* Correlating Microstructural Lithium Metal Growth with Electrolyte Salt Depletion in Lithium Batteries Using ^{7}Li MRI. *J. Am. Chem. Soc.* **137**, 15209–15216 (2015).
10. Brissot, C., Rosso, M., Chazalviel, J.-N. & Lascaud, S. Dendritic growth mechanisms in lithium/polymer cells. *J. Power Sources* **81–82**, 925–929 (1999).
11. Peled, E. & Menkin, S. Review—SEI: Past, Present and Future. *J. Electrochem. Soc.* **164**, A1703–A1719 (2017).
12. Aurbach, D. Review of selected electrode–solution interactions which determine the performance of Li and Li ion batteries. *J. Power Sources* **89**, 206–218 (2000).
13. Yoon, G., Moon, S., Ceder, G. & Kang, K. Deposition and Stripping Behavior of Lithium Metal in Electrochemical System: Continuum Mechanics Study. *Chem. Mater.* **30**, 6769–6776 (2018).
14. Aurbach, D., Weissman, I., Schechter, A. & Cohen, H. X-ray Photoelectron Spectroscopy Studies of Lithium Surfaces Prepared in Several Important Electrolyte Solutions. A Comparison with Previous Studies by Fourier Transform Infrared Spectroscopy. *Langmuir* **12**, 3991–4007 (1996).
15. Xu, C. *et al.* Improved Performance of the Silicon Anode for Li-Ion Batteries: Understanding the Surface Modification Mechanism of Fluoroethylene Carbonate as an Effective Electrolyte Additive. *Chem. Mater.* **27**, 2591–2599 (2015).
16. Lu, P. & Harris, S. J. Lithium transport within the solid electrolyte interphase. *Electrochim. commun.* **13**, 1035–1037 (2011).
17. Haber, S. & Leskes, M. What Can We Learn from Solid State NMR on the Electrode–Electrolyte Interface? *Adv. Mater.* **30**, (2018).
18. Pecher, O., Carretero-González, J., Griffith, K. J. & Grey, C. P. Materials’ Methods: NMR in Battery Research. *Chem. Mater.* **29**, 213–242 (2017).
19. Becerra, L. R. *et al.* A Spectrometer for Dynamic Nuclear Polarization and Electron Paramagnetic Resonance at High Frequencies. *J. Magn. Reson. Ser. A* **117**, 28–40 (1995).

20. Thankamony, A. S. L., Wittmann, J. J., Kaushik, M. & Corzilius, B. Dynamic nuclear polarization for sensitivity enhancement in modern solid-state NMR. *Prog. Nucl. Magn. Reson. Spectrosc.* **102–103**, 120–195 (2017).
21. Kemp, T. F. *et al.* Dynamic nuclear polarization enhanced NMR at 187 GHz/284 MHz using an extended interaction Klystron amplifier. *J. Magn. Reson.* **265**, 77–82 (2016).
22. Leskes, M. *et al.* Surface-Sensitive NMR Detection of the Solid Electrolyte Interphase Layer on Reduced Graphene Oxide. *J. Phys. Chem. Lett.* **8**, 1078–1085 (2017).
23. Jin, Y. *et al.* Identifying the Structural Basis for the Increased Stability of the Solid Electrolyte Interphase Formed on Silicon with the Additive Fluoroethylene Carbonate. *J. Am. Chem. Soc.* **139**, 14992–15004 (2017).
24. Jin, Y. *et al.* Understanding Fluoroethylene Carbonate and Vinylene Carbonate Based Electrolytes for Si Anodes in Lithium Ion Batteries with NMR Spectroscopy. *J. Am. Chem. Soc.* **140**, 9854–9867 (2018).
25. Berruyer, P., Emsley, L. & Lesage, A. DNP in Materials Science : Touching the Surface. *eMagRes* **7**, 93–104 (2018).
26. Wolf, T. *et al.* Endogenous Dynamic Nuclear Polarization for Natural Abundance ^{17}O and Lithium NMR in the Bulk of Inorganic Solids. *J. Am. Chem. Soc.* **141**, 451–462 (2018).
27. Carver, T. R. & Slichter, C. P. Polarization of Nuclear Spins in Metals. *Phys. Rev.* **92**, 212–213 (1953).
28. Overhauser, A. W. Polarization of Nuclei in Metals. *Phys. Rev.* **92**, 411–415 (1953).
29. Feher, G. & Kip, A. F. Electron spin resonance absorption in metals. I. Experimental. *Phys. Rev.* **98**, 337–348 (1955).
30. Michan, A. L., Leskes, M. & Grey, C. P. Voltage Dependent Solid Electrolyte Interphase Formation in Silicon Electrodes: Monitoring the Formation of Organic Decomposition Products. *Chem. Mater.* **28**, 385–398 (2016).
31. Gullion, T. & Schaefer, J. Rotational-echo double-resonance NMR. *J. Magn. Reson.* **81**, 196–200 (1989).
32. Markevich, E., Salitra, G., Chesneau, F., Schmidt, M. & Aurbach, D. Very Stable Lithium Metal Stripping–Plating at a High Rate and High Areal Capacity in Fluoroethylene Carbonate-Based Organic Electrolyte Solution. *ACS Energy Lett.* **2**, 1321–1326 (2017).
33. Brown, Z. L., Jurng, S., Nguyen, C. C. & Lucht, B. L. Effect of Fluoroethylene Carbonate Electrolytes on the Nanostructure of the Solid Electrolyte Interphase and Performance of Lithium Metal Anodes. *ACS Appl. Energy Mater.* **1**, 3057–3062 (2018).
34. Fang, C. *et al.* Quantifying inactive lithium in lithium metal batteries. *Nature* **572**, 511–515 (2019).
35. Heine, J. *et al.* Fluoroethylene Carbonate as Electrolyte Additive in Tetraethylene Glycol Dimethyl Ether Based Electrolytes for Application in Lithium Ion and Lithium Metal Batteries. *J. Electrochem. Soc.* **162**, A1094–A1101 (2015).
36. Michan, A. L. *et al.* Fluoroethylene carbonate and vinylene carbonate reduction: Understanding lithium-ion battery electrolyte additives and solid electrolyte interphase formation. *Chem. Mater.* **28**, 8149–8159 (2016).
37. Shkrob, I. A., Wishart, J. F. & Abraham, D. P. What Makes Fluoroethylene Carbonate Different? *J. Phys. Chem. C* **119**, 14954–14964 (2015).

38. Bennett, L. H., Watson, R. E. & Carter, G. C. Relevance of knight shift measurements to the electronic density of states. *J. Res. Natl. Bur. Stand. Sect. A Phys. Chem.* **74A**, 569–610 (1970).
39. Pressley, R. J. & Berk, H. L. g Factor of Conduction Electrons in Metallic Lithium. *Phys. Rev.* **140**, A1207–A1210 (1965).
40. Lesseux, G. G. *et al.* Unusual diffusive effects on the ESR of Nd³⁺ ions in the tunable topologically nontrivial semimetal YBiPt. *J. Phys. Condens. Matter* **28**, 125601 (2016).
41. Leskes, M., Moore, A. J., Goward, G. R. & Grey, C. P. Monitoring the electrochemical processes in the lithium-air battery by solid state NMR spectroscopy. *J. Phys. Chem. C* **117**, 26929–26939 (2013).
42. Meyer, B. M., Leifer, N., Sakamoto, S., Greenbaum, S. G. & Grey, C. P. High Field Multinuclear NMR Investigation of the SEI Layer in Lithium Rechargeable Batteries. *Electrochem. Solid-State Lett.* **8**, A145 (2005).
43. Hu, Y.-Y. *et al.* Origin of additional capacities in metal oxide lithium-ion battery electrodes. *Nat. Mater.* **12**, 1130–1136 (2013).
44. Aurbach, D. A Comparative Study of Synthetic Graphite and Li Electrodes in Electrolyte Solutions Based on Ethylene Carbonate-Dimethyl Carbonate Mixtures. *J. Electrochem. Soc.* **143**, 3809 (1996).
45. Sloop, S. E., Pugh, J. K., Wang, S., Kerr, J. B. & Kinoshita, K. Chemical Reactivity of PF₅ and LiPF₆ in Ethylene Carbonate/Dimethyl Carbonate Solutions. *Electrochem. Solid-State Lett.* **4**, A42 (2001).
46. Kittel, C. *Introduction to Solid State Physics*. (John Wiley & Sons, 2004).
47. Pifer, J. H. & Magno, R. Conduction-Electron Spin Resonance in a Lithium Film. *Phys. Rev. B* **3**, 663–673 (1971).
48. Palenskis, V. Drift Mobility, Diffusion Coefficient of Randomly Moving Charge Carriers in Metals and Other Materials with Degenerated Electron Gas. *World J. Condens. Matter Phys.* **03**, 73–81 (2013).
49. Pecher, O., Vyalikh, A. & Grey, C. P. Challenges and new opportunities of in situ NMR characterization of electrochemical processes. *AIP Conf. Proc.* **1765**, (2016).
50. Freytag, A. I., Pauric, A. D., Krachkovskiy, S. A. & Goward, G. R. In Situ Magic-Angle Spinning ⁷Li NMR Analysis of a Full Electrochemical Lithium-Ion Battery Using a Jelly Roll Cell Design. *J. Am. Chem. Soc.* **141**, 13758–13761 (2019).
51. Massiot, D. *et al.* Modelling one- and two-dimensional solid-state NMR spectra. *Magn. Reson. Chem.* **40**, 70–76 (2002).
52. Lide, D. R. *CRC Handbook of Chemistry and Physics*. (CRC Press, 2003).

Supplementary Information

DNP-enhanced NMR of Lithium Dendrites: Selective Observation of the Solid–Electrolyte Interphase

Michael A. Hope,¹ Bernardine L. D. Rinkel,¹ Anna B. Gunnarsdóttir,¹ Katharina Märker,¹ Svetlana Menkin,¹ Subhradip Paul,² Ivan Sergeyev,³ Clare P. Grey¹

1. Department of Chemistry, University of Cambridge, Lensfield Road, Cambridge, CB2 1EW, U.K
2. School of Physics and Astronomy, University of Nottingham, University Park, Nottingham, NG7 2RD, U.K
3. Bruker Biospin Corp., 15 Fortune Drive, Billerica, MA, 01821, USA.

Experimental

Copper metal disks (MTI) were soaked in concentrated acetic acid for 10 minutes for oxide removal. The acetic acid residue was removed with dry nitrogen flow and the disks were dried at 100 °C under vacuum overnight. The lithium metal disks (LTS research, 99.95%) were used without any pretreatment. Printed LiNi_{0.8}Mn_{0.1}Co_{0.1}O₂ (NMC811) electrodes were fabricated in Argonne National Laboratory (A-C020, made by CAMP facility) using the following materials: 90 wt % NMC811 (Targray), 5 wt % conductive carbon (Timcal C45), and 5 wt % PVDF binder (Solvay 5130). They were dried overnight at 120°C under dynamic vacuum.

Li–Li, Li–Cu and NMC811–Cu coin cells were assembled in an Ar atmosphere glovebox (O₂, H₂O < 1 ppm, MBraun) in stainless-steel 2032 coin cells (Cambridge Energy Solutions) with a stainless-steel conical spring, two 0.5 mm thick stainless-steel spacer disks and polypropylene-polyethylene separator (Celgard 3501, dried under vacuum at 40°C). For NMC811–Cu cells, an additional glass fibre separator (GF/B, Whatman) was used on the NMC811 side. The coin cell components were dried for at least a week at 60 °C. The electrolyte consisted of 75 µL of 1 M LiPF₆ in ethylene carbonate/dimethyl carbonate 1:1 vol (EC:DMC; Sigma Aldrich, battery grade), referred to as LP30, and the same electrolyte with 10% vol of the additive fluoroethylene carbonate (FEC; Sigma Aldrich, anhydrous), referred to as LP30+FEC.

Galvanostatic electrodeposition was performed using a Biologic VSP potentiostat with EC-Laboratory software. The constant currents shown in Table S1 were applied in a single direction for a capacity of 4 mAh/cm². The coin cells were disassembled in an Ar atmosphere glovebox and the microstructures scraped off gently with a razorblade without rinsing. The sample was then diluted by ~5× by mass with dry KBr to improve microwave penetration and allow the metallic samples to be more easily spun, before packing into a 3.2 mm outer diameter sapphire rotor.

For the NMR experiments performed at 14.1 T, radiofrequency (rf) powers were used of 45 kHz for ⁷Li, 110 kHz for ¹H and 85 kHz for ¹⁹F. For the CP experiments, rf powers during contact were used of ~45 kHz for ⁷Li, ~85 kHz for ¹H and ~70 kHz for ¹⁹F. The experiments at 9.4 T used a ⁷Li rf power of 100 kHz. ¹H NMR spectra were referenced to adamantane at 1.81 ppm, ⁷Li spectra to LiF at -1 ppm and ¹⁹F spectra to LiF at -203 ppm, all at room temperature. The gyrotron microwave powers were measured using a calorimeter half-way along the waveguide, while the klystron power was measured at the output using a directional coupler then scaled to account for microwave reflection. Spectra were deconvoluted using dmfit software.⁵¹

Continuous-wave X-band ESR measurements were performed on pieces of lithium metal on a Bruker E500 X-band spectrometer with an ER 4122SHQE cavity, tuned to 9.373 GHz. The external magnetic field was modulated at 100 kHz with a modulation amplitude of 1 G.

Table S1: Summary of different microstructural lithium samples used in this work.

Substr.	Electrolyte	Current density /mA cm ⁻²	Experiments
A	Li	LP30+FEC	1.25 ⁷ Li metal spectra, RT and 100 K. RT field sweep.
B	Cu	LP30	0.033 100 K full field sweep. Metal spectra as a function of microwave power.
C	Cu*	LP30	0.455 ⁷ Li experiments at 9.4 T.
D	Li	LP30	1.25 Main text comparison of electrolytes.
E	Li	LP30+FEC	1.25 Main text comparison of electrolytes. Enhancement as a function of T and power.
F	Li	LP30	1.25 SI comparison of electrolytes.
G	Li	LP30+FEC	1.25 SI comparison of electrolytes. Field sweeps for different µw powers.

* NMC811 used as the Li source. All other samples used Li metal.

Table S2: Recycle delays, number of scans and experimental time for the experiments shown in Figure 2 in the main text.

	Experiment	Recycle delay /s	Scans	Experimental time
a – d	Diamagnetic ⁷ Li	1	32	32 s
e	Direct ¹ H, LP30	10	16	2 min 41 s
g	Direct ¹ H, LP30+FEC	10	32	5 min 23 s
i	Direct ¹⁹ F, LP30	30	4	2 min
k	Direct ¹⁹ F, LP30+FEC	3	32	1 min 37 s
f, h, j, l	⁷ Li→ ¹ H and ⁷ Li→ ¹⁹ F CP	1	320	5 min 44 s

Skin Depth Calculation

The skin depth for penetration of electromagnetic radiation into a metal is given by:⁴⁶

$$d = \sqrt{\frac{\rho}{\pi\mu_0\mu_r\nu}} \quad (S1)$$

where ρ the resistivity of the metal (92.8 nΩ m for Li metal at 293 K⁵²), μ_0 is the vacuum permeability, μ_r is the relative permeability (1.4 for Li metal⁵²) and ν is the frequency of the radiation.

For the radiofrequency and microwave radiation used at 14.1 T in this study, this yields the skin depths shown in Table S3. At lower temperatures the resistivity decreases, resulting in a shallower skin depth.

Table S3: Skin depths for the radiofrequency and microwave penetration of Li metal.

Radiation	Frequency	Skin depth, 300 K	Skin depth, 100 K
Radiofrequency	233 MHz	8.6 μm	3.7 μm
Microwave	395 GHz	0.21 μm	0.09 μm

Additional Data and Figures

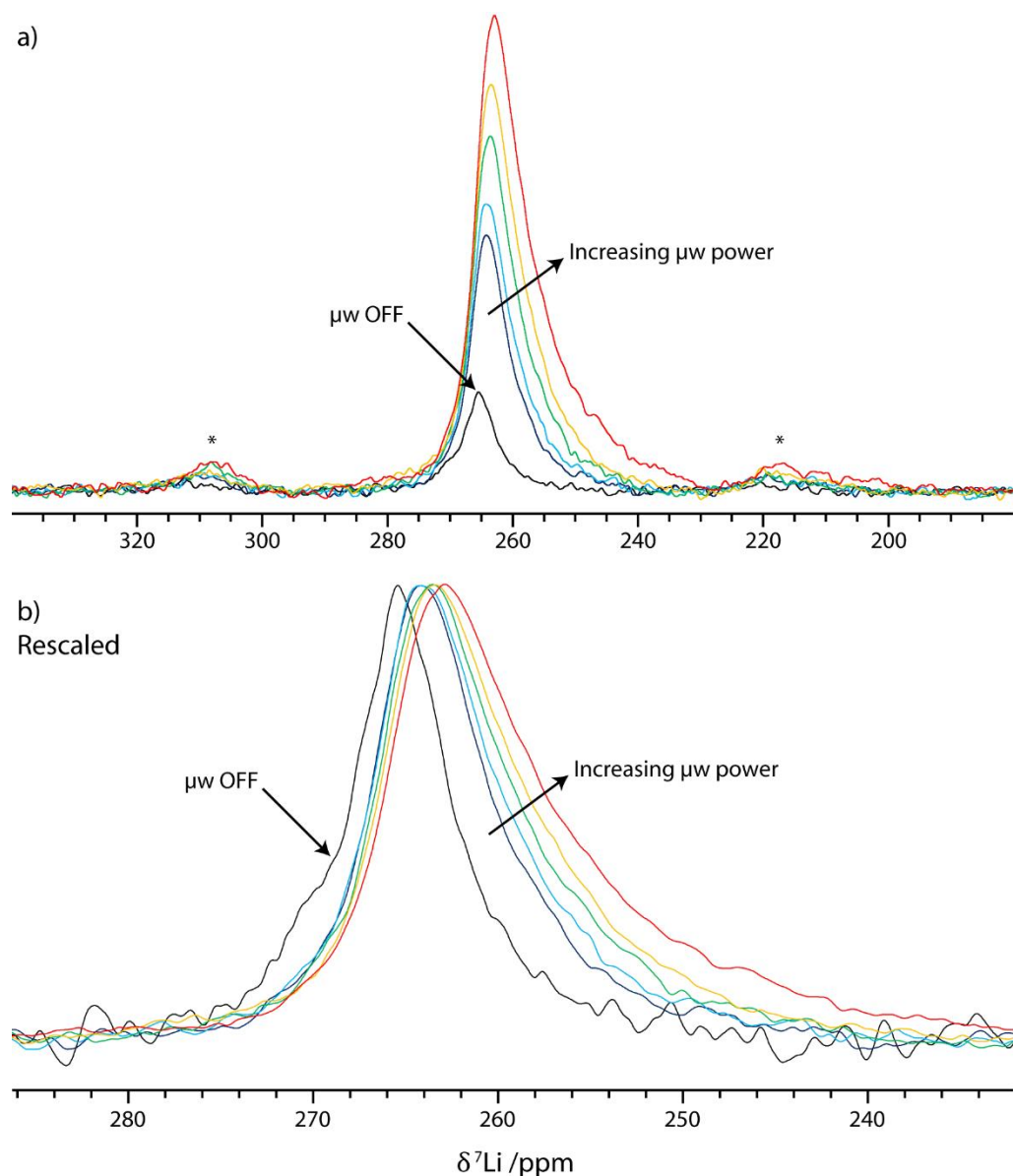


Figure S1: ${}^7\text{Li}$ NMR spectrum of microstructural lithium metal (sample B) without microwave irradiation ($\mu\text{w OFF}$) and as a function of microwave power (7.4, 8.7, 11.0, 13.2 and 15.6 W), recorded at 14.1 T, 10 kHz MAS and a sample temperature of ~100 K, using a Hahn echo pulse sequence and a recycle delay of 0.1 s. Spinning sidebands are marked with an asterisk. The spectra in b) have been rescaled to all have the same intensity, to allow easier comparison of the average chemical shifts.

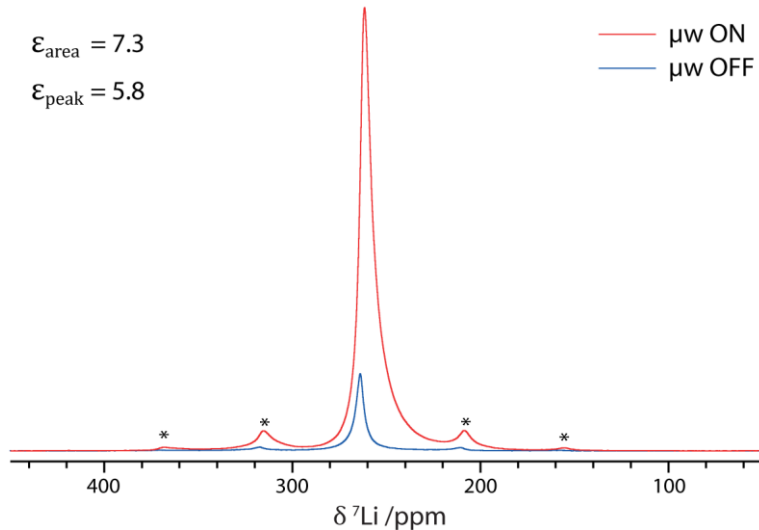


Figure S2: ${}^7\text{Li}$ NMR spectrum of microstructural lithium metal (sample A), with and without 15.6 W of microwave irradiation at 395.29 GHz ($\mu\text{w ON/OFF}$), recorded at 14.1045 T, 12.5 kHz MAS and a sample temperature of \sim 100 K, using a Hahn echo pulse sequence and a recycle delay of 0.25 s. Spinning sidebands are marked with an asterisk.

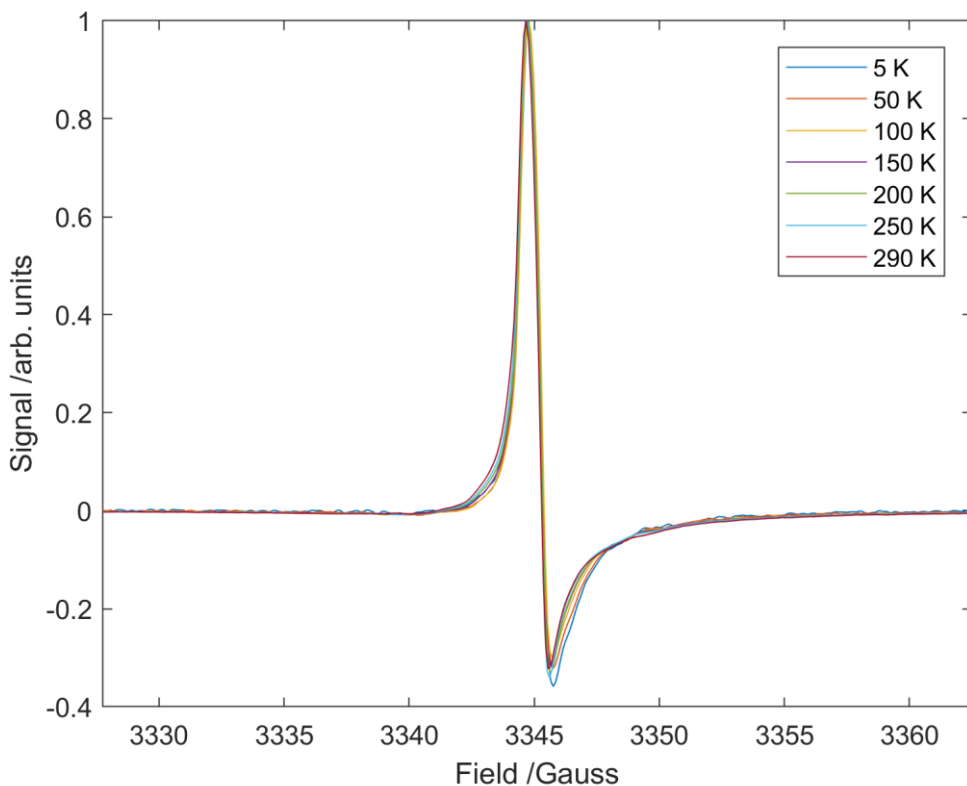


Figure S3: The X-band ($v = 9.376393$ GHz) EPR spectra of lithium metal as a function of temperature, showing the expected Dysonian lineshape. The microwave frequency changed slightly as a function of temperature, so the magnetic field axes of the low temperature spectra have been rescaled to the 290 K frequency to allow comparison of the spectra, and the intensities have been scaled to the same maximum. The peak absorbance (derivative = 0) occurs at $B_0 = 3345.268$ G, corresponding to $g = 2.0026$.

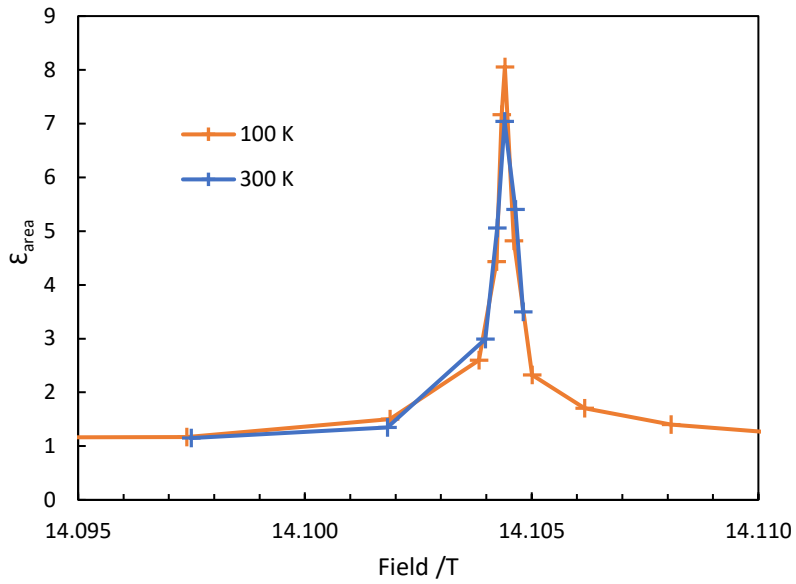


Figure S4: The enhancement of the integrated intensity for the metal ${}^7\text{Li}$ NMR signal of microstructural lithium as a function of the B_0 field, measured at 100 K (sample B, Figure 1b, main text) and 300 K (sample A), with microwave irradiation at 395.29 GHz and 16.5 W, recorded at 12.5 kHz MAS with a recycle delay of 0.25 s.

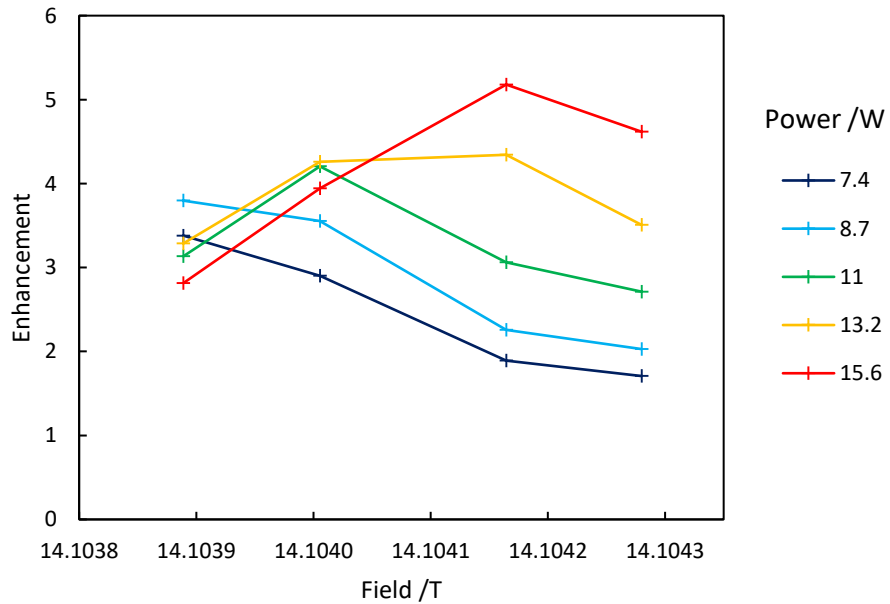


Figure S5: The enhancement of the integrated intensity for the metal ${}^7\text{Li}$ NMR signal of microstructural lithium (sample G) as a function of the B_0 field, measured at room temperature, with microwave irradiation at 395.29 GHz and different powers, recorded at 12.5 kHz MAS with a recycle delay of 0.25 s. As the microwave power increases, the field at which maximal enhancement occurs increases.

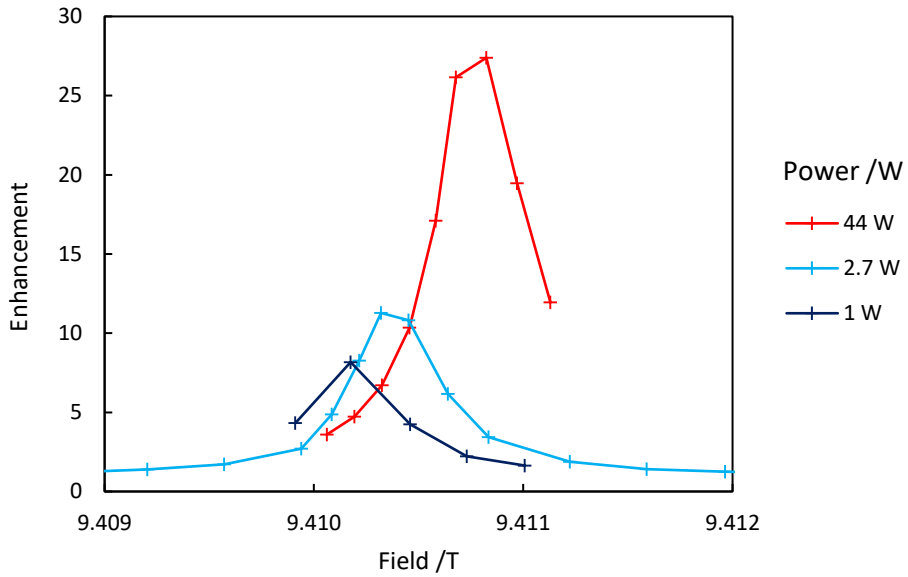


Figure S6: The enhancement of the integrated intensity for the metal ${}^7\text{Li}$ NMR signal of microstructural lithium (sample C) as a function of the B_0 field, measured at 100 K with different microwave powers, 8 kHz MAS and a recycle delay of 0.25 s. The 44 W profile was recorded with gyrotron irradiation at 263.7 GHz gyrotron, while the 2.7 and 1.0 W profiles were recorded with a 264.6 GHz klystron. The klystron profiles have been shifted to coincide with the corresponding fields for 263.7 GHz.

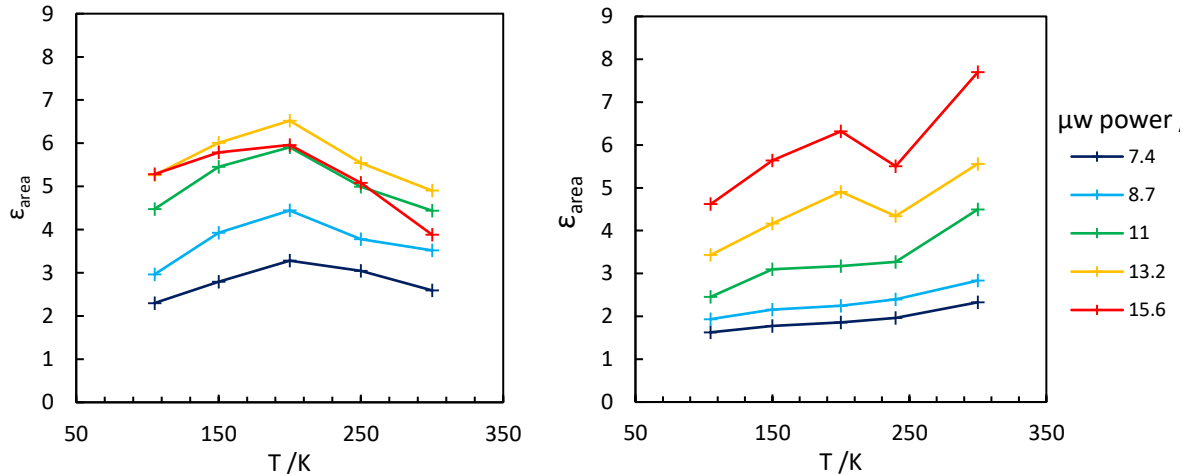


Figure S7: Enhancement, by area, of the microstructural ${}^7\text{Li}$ metal signal (sample E) as a function of temperature for different microwave powers. Recorded at 12.5 kHz MAS and 14.1039 T (left) or 14.1042 T (right).

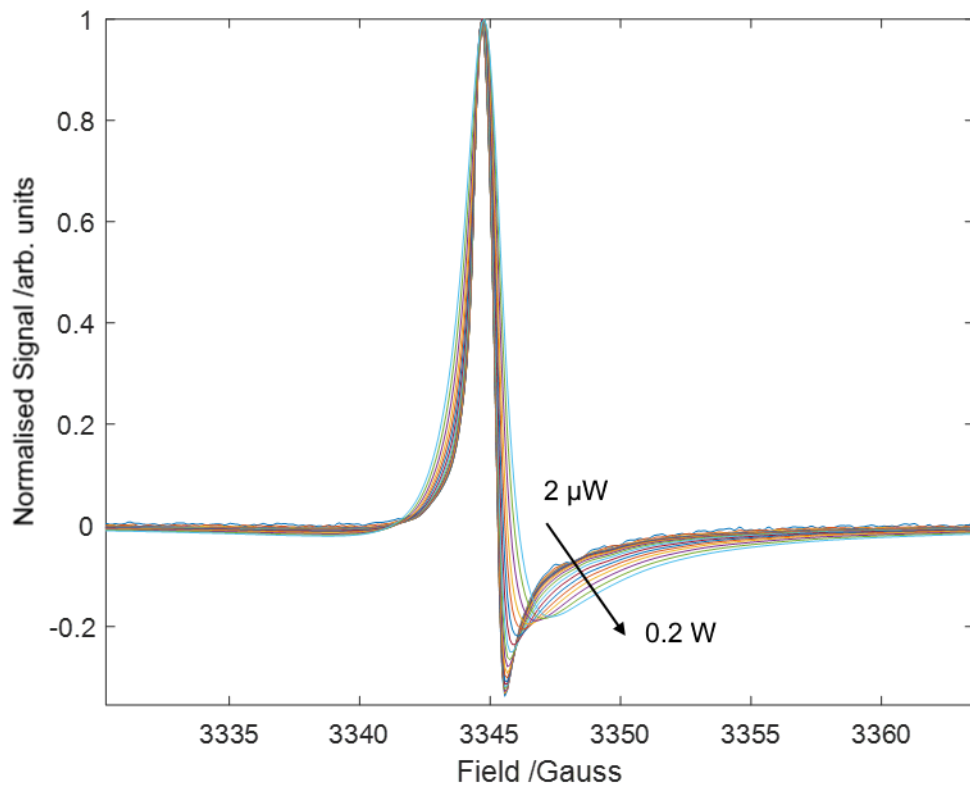


Figure S8: The room temperature X-band ($\nu = 9.376393$ GHz) EPR spectra of lithium metal as a function of power, logarithmically spaced between $2 \mu\text{W}$ and 0.2 W . The intensities been normalised to the same maximum value.

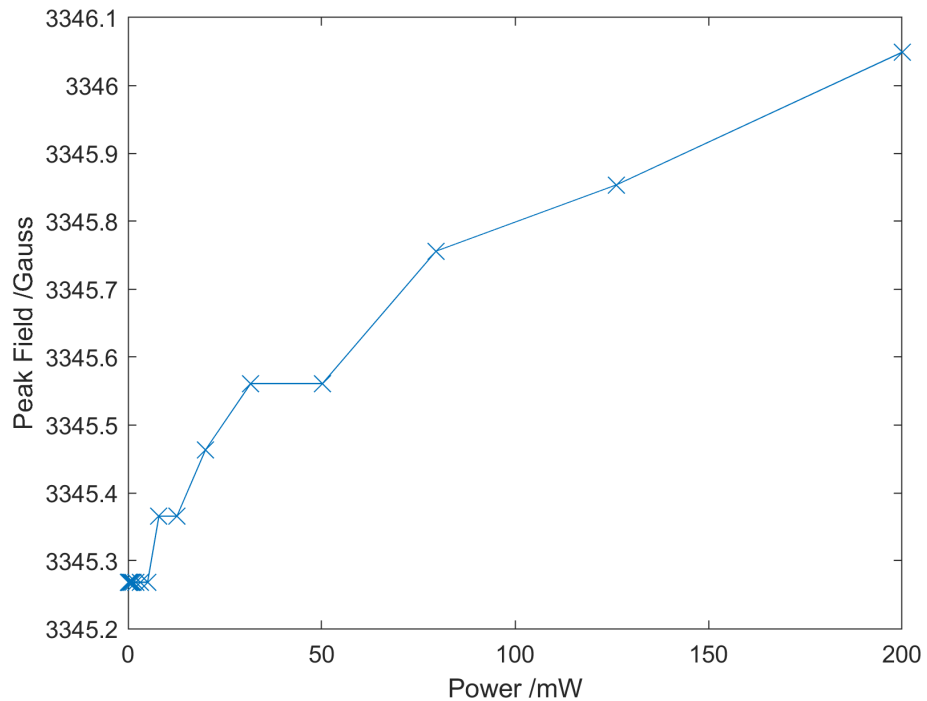


Figure S9: Magnetic field at peak absorbance (derivative = 0) as a function of microwave power for the EPR spectra of lithium metal at room temperature and $\nu = 9.376393$ GHz. Spectra shown in Figure S8.

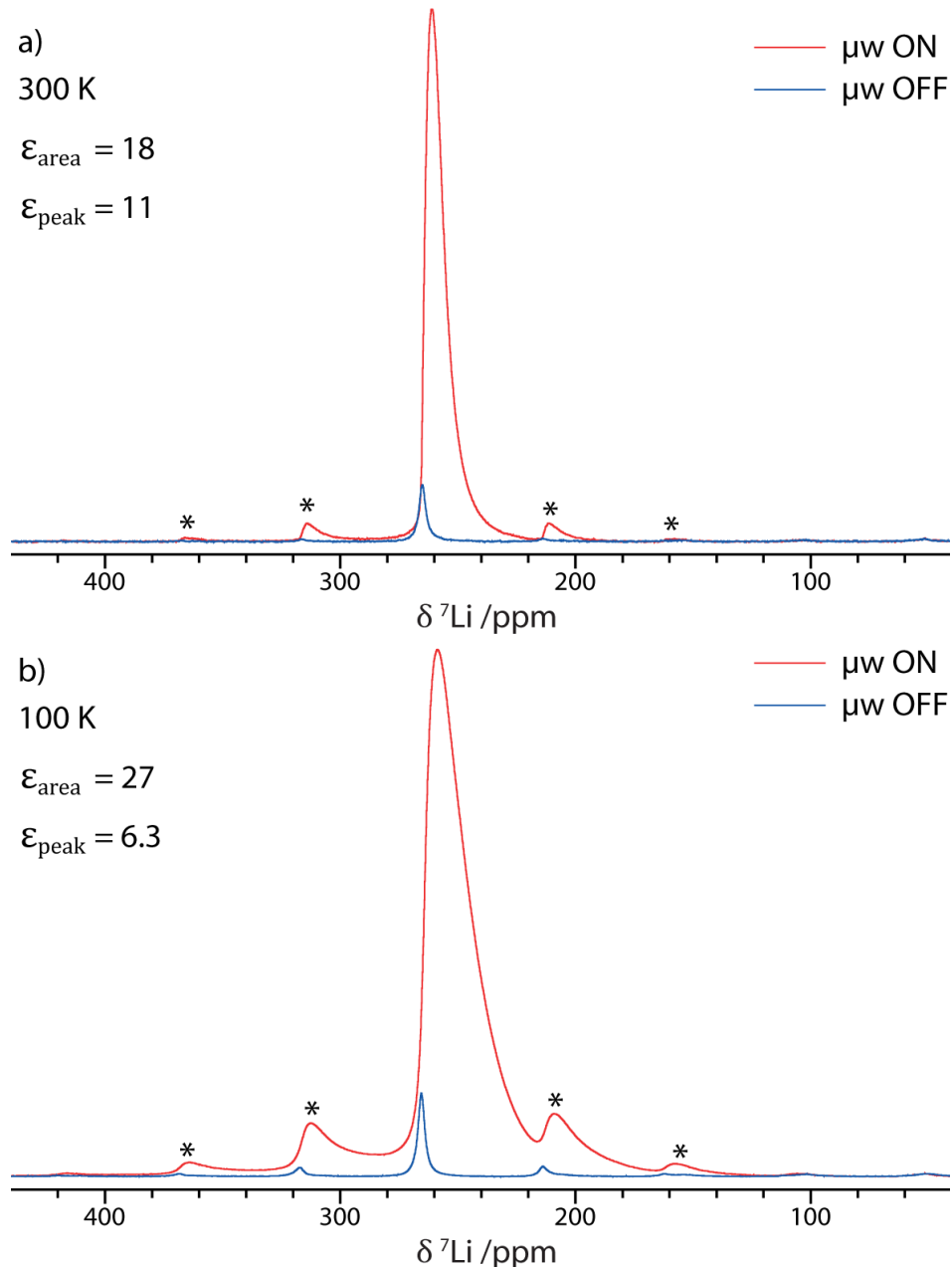


Figure S10: ^7Li NMR spectrum of microstructural lithium metal (sample C), with and without 44 W of gyrotron microwave irradiation at 263.7 GHz ($\mu\text{w ON/OFF}$), recorded at 9.4 T, 8 kHz MAS and samples temperatures of a) ~ 100 K and b) ~ 300 K, using a Hahn echo pulse sequence and a recycle delay of 0.25 s. Spinning sidebands are marked with an asterisk.

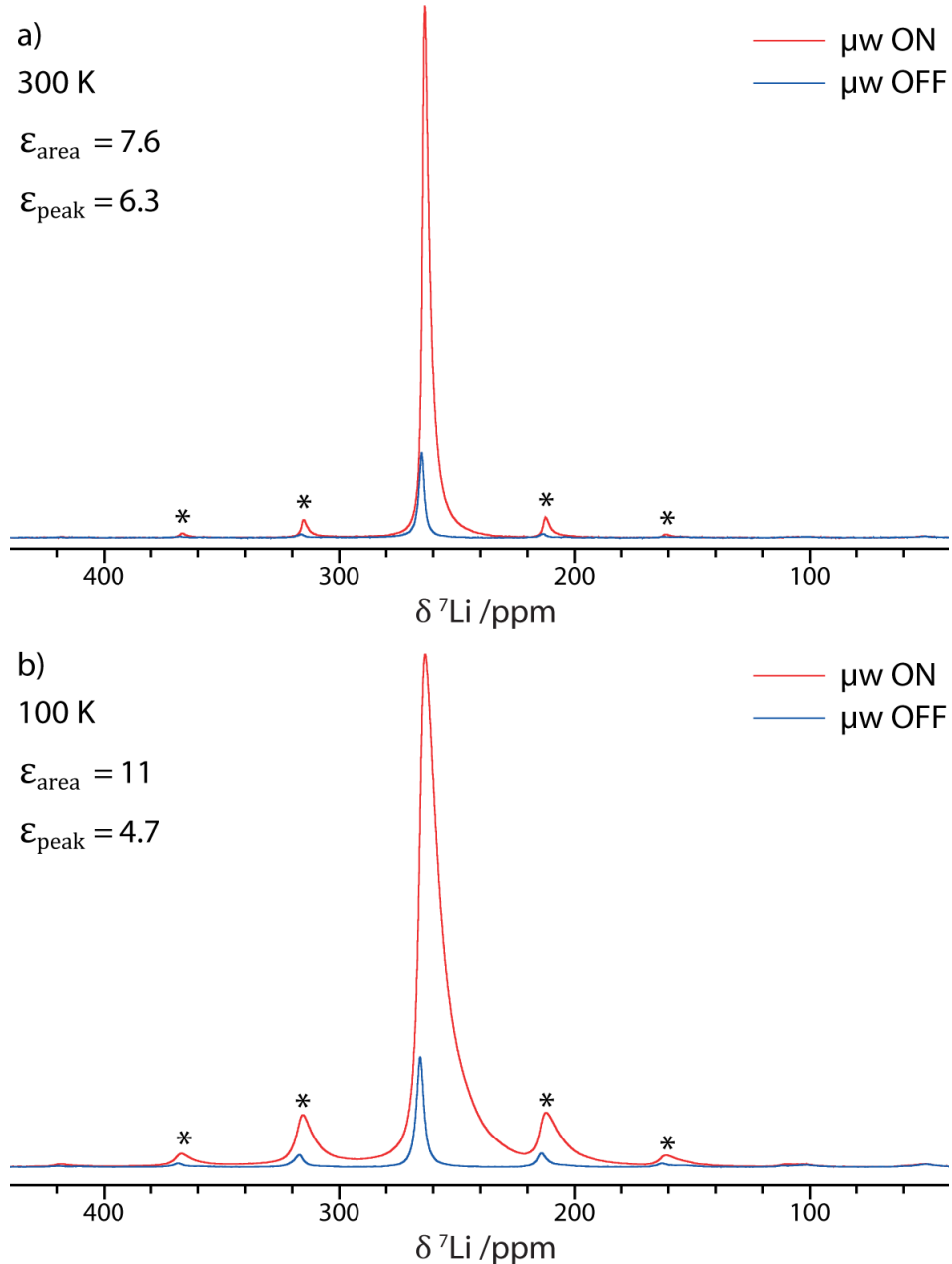


Figure S11: ${}^7\text{Li}$ NMR spectrum of microstructural lithium metal (sample C), with and without ~ 2.7 W of klystron microwave irradiation at 264.6 GHz ($\mu\text{w ON/OFF}$), recorded at 9.4 T, 8 kHz MAS and samples temperatures of a) ~ 100 K and b) ~ 300 K, using a Hahn echo pulse sequence and a recycle delay of 0.25 s. Spinning sidebands are marked with an asterisk.

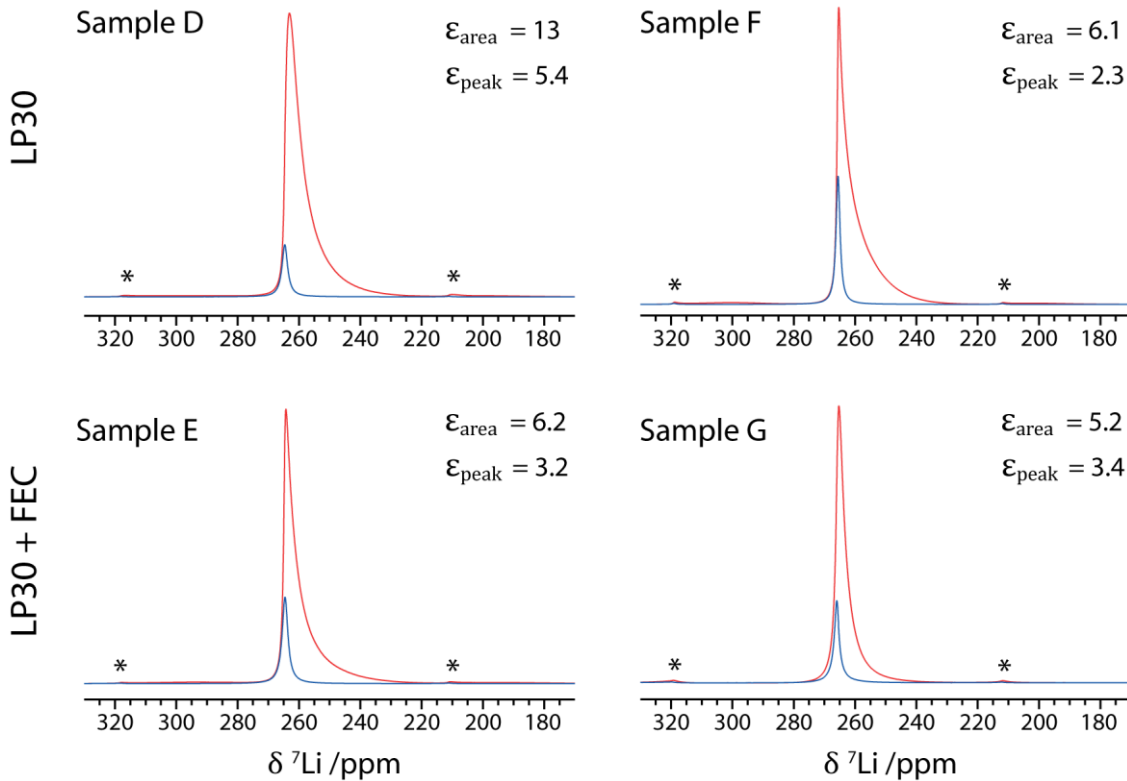


Figure S12: ${}^7\text{Li}$ NMR spectra for both sets of microstructural lithium samples (D – G), deposited using the LP30 and LP30+ FEC electrolytes, with and without microwave irradiation at 395.29 GHz ($\mu\text{w ON/OFF}$; 15.6 W for D, E and 11.0 W for F, G), recorded at 14.1 T, 12.5 kHz MAS and room temperature, using a Hahn echo pulse sequence and a recycle delay of 0.25 s. Spinning sidebands are marked with an asterisk.

Table S4: Enhancements and T_1 and T_{DNP} build-up constants, where measured, for the metal ${}^7\text{Li}$ signal for different microstructural lithium samples. T_1 and T_{DNP} were measured with saturation recovery experiments with and without microwave irradiation, respectively.

Sample	Field /T	ν_{MAS} /kHz	$\mu\text{w power}$ /W	T /K	$\varepsilon_{\text{area}}$	T_1 /s	T_{DNP} /s
A	14.1	12.5	15.6	100	7.3	–	–
				300	7.9	0.14	0.13
B	14.1	10	15.6	100	8.1	–	0.25
C	9.4	8	2.7 44	100	11	0.45	0.31
				300	7.6	–	0.13
				100	27	–	–
				300	18	–	–
D	14.1	12.5	15.6	300	13	–	–
E	14.1	12.5	15.6	300	6.2	–	–
F	14.1	12.5	11.0	300	6.1	–	–
G	14.1	12.5	11.0	100	10	0.36	0.31
			15.6	300	5.2	0.14	0.13

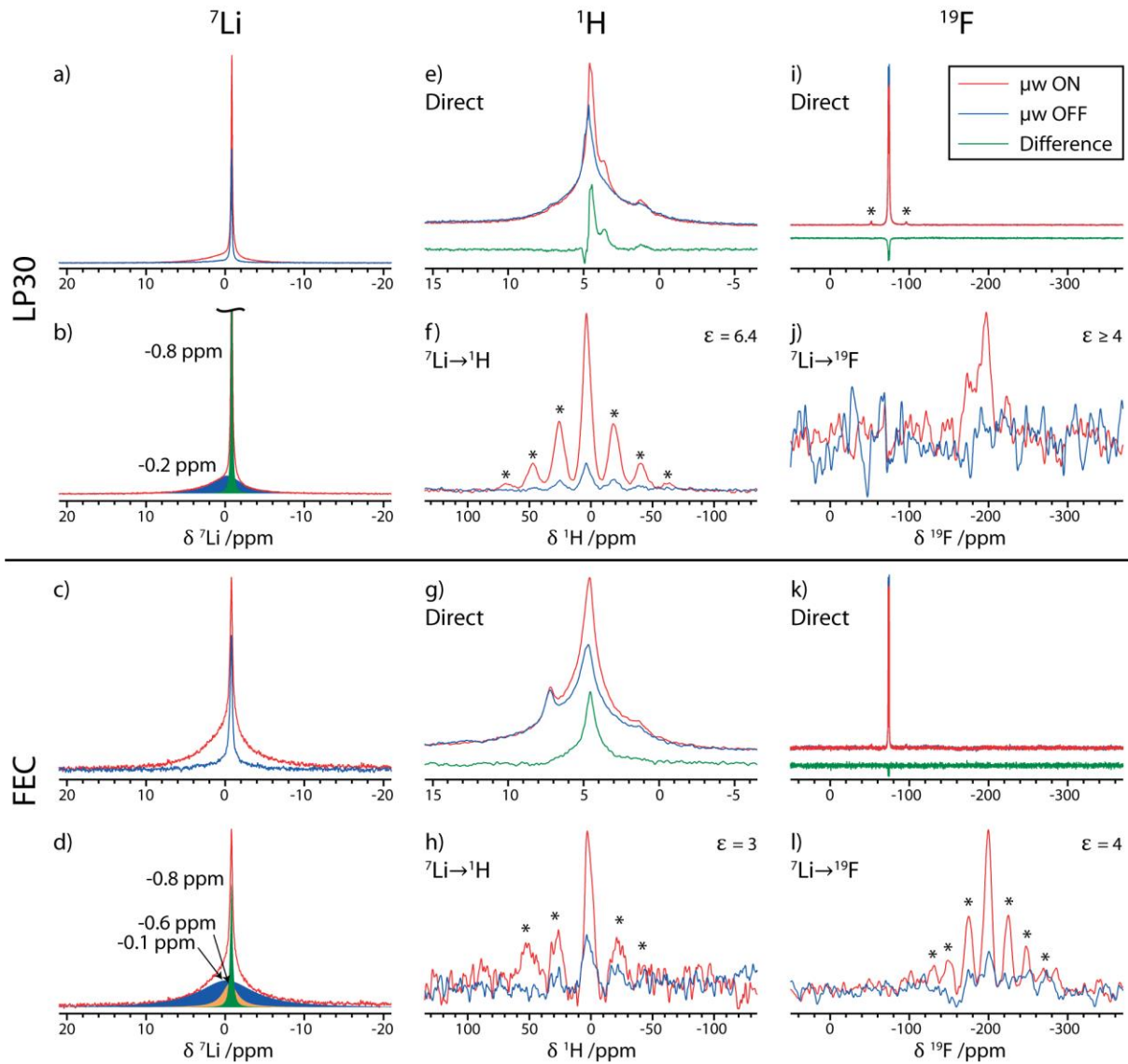


Figure S13: Diamagnetic ^7Li (a–d), ^1H (e–h), and ^{19}F (i–l) NMR spectra of lithium microstructures produced by cycling with the LP30 (sample F, top half) and LP30+FEC (sample G, bottom half) electrolytes, recorded with and without microwave irradiation ($\mu\text{w ON/OFF}$; 11.0 W for a–i, 15.6 W for j–l). All spectra were recorded at 12.5 kHz MAS, 14.1 T and room temperature, unless otherwise stated; spinning sidebands are marked with asterisks. The direct spectra were recorded with a Hahn echo pulse sequence and the CP spectra were recorded with the ^7Li carrier at 0 ppm and contact times of 1 ms and 0.1 ms for $^7\text{Li} \rightarrow ^1\text{H}$ and $^7\text{Li} \rightarrow ^{19}\text{F}$ respectively. For the direct ^1H and ^{19}F experiments, the difference between the spectra recorded with and without microwave irradiation is also shown. The recycle delays were: 1 s (a – d, e, f, h, j, l); 3 s (i, k); or 45 s (g).

Table S5: Deconvolution and DNP enhancements (ϵ) of the direct ^1H NMR spectra (main text, Figure 2e,g) of microstructural lithium deposited using the LP30 and LP30 + FEC electrolytes (samples D and E). The deconvoluted spectra are shown in Figure S17 and Figure S18. The enhancements are given by the ratio of the microwave off and on spectra; if the signal could not be easily distinguished in the microwave-off spectrum, the microwave-off intensity was calculated by subtracting the deconvoluted intensity in the difference spectrum from that of the microwave-on spectrum.

LP30								
Chemical shift /ppm	0.10	1.26	3.8	3.87	4.68	4.68	4.74	7.27
FWHM /ppm ^a	0.15	1.10	0.094	0.55	3.93	0.12	0.52	0.09
Integration /% ^b	2.50	3.84	0.29	2.26	68.66	6.55	13.82	2.07
ϵ	1.0	1.3	1.9	∞^b	1.1	2.0	1.8	0.9
LP30 + FEC								
Chemical shift /ppm	0.17	1.00	1.39	1.70	2.14	4.50	4.71	7.22
FWHM /ppm ^a	0.5	0.28	0.22	0.2	0.32	7.58	1.82	0.37
Integration ^b	0.05	84.16	0.15	0.03	0.04	8.82	6.64	0.12
ϵ	1.1	1.2	1.5	1.5	1.4	1.0	1.3	0.7

^aFull-width at half-maximum

^bThis signal could not be seen in the microwave-off spectrum, and the intensity in the difference spectrum is the same as in the microwave-on spectrum within error.

Table S6: Deconvolution and DNP enhancements (ϵ) of the diamagnetic ^7Li signals (Figure S13b,d) of microstructural lithium deposited from the LP30 and LP30+FEC electrolytes (samples F and G). There is some additional error introduced to the fits due to field drift and an imperfect shim.

	LP30		LP30 + FEC		
Shift /ppm	-0.8	-0.2	-0.8	-0.6	-0.1
FWHM /ppm	0.18	4.5	0.35	2.3	8.5
Integration /%	45	55	14	17	69
ϵ	1.9	4.0	1.2	3.7	4.4

Table S7: Deconvolution and DNP enhancements (ϵ) of the direct ^1H NMR spectra (Figure S13e,g) of microstructural lithium deposited using the LP30 and LP30+FEC electrolytes (samples F and G). The enhancements are calculated either from the ratio of the microwave off and on spectra, or from the intensity in the difference spectrum if the signal could not be easily distinguished in the microwave-off spectrum.

	LP30				LP30 + FEC			
Shift /ppm	1.32	3.8	4.6	4.73	1.33	4.48	4.65	7.23
FWHM /ppm	0.93	0.56	4.78	0.57	0.65	6.69	0.91	0.45
Integration /%	4.3	4.6	63.8	27.3	1.1	69.9	26.0	3.0
ϵ	2.0	∞^a	1.0	1.7	$\sim 1.4 - 2.7$	1.1	1.8	0.9

^aThis signal could not be seen in the microwave off spectrum, and the intensity in the difference spectrum is the same as in the microwave on spectrum.

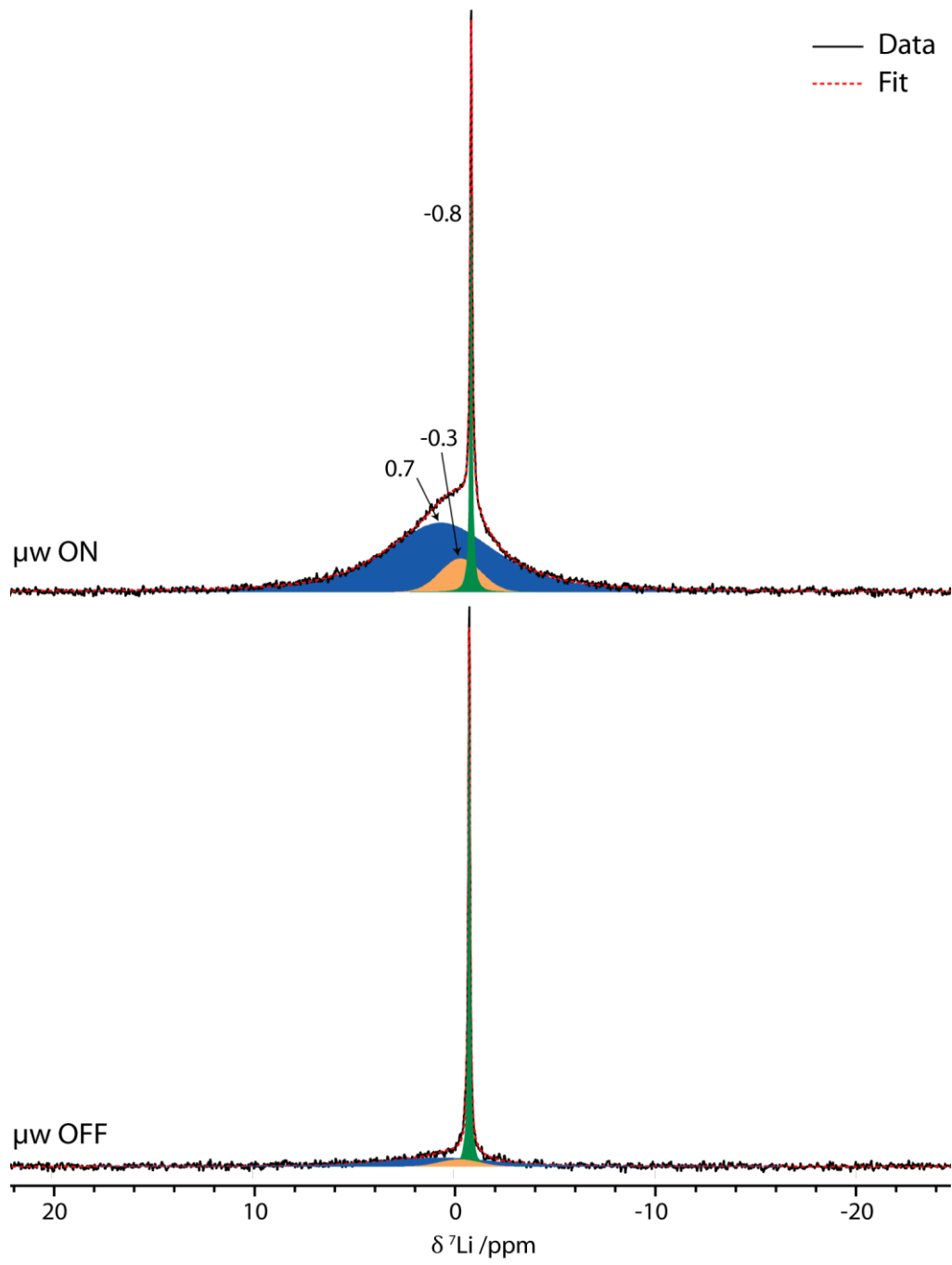


Figure S14: Deconvoluted ${}^7\text{Li}$ NMR spectra with and without microwave irradiation for microstructural lithium deposited with the LP30 electrolyte (sample D, Figure 2b), recorded at room temperature, 14.1 T and 12.5 kHz MAS with a 1 s recycle delay and a Hahn echo pulse sequence.

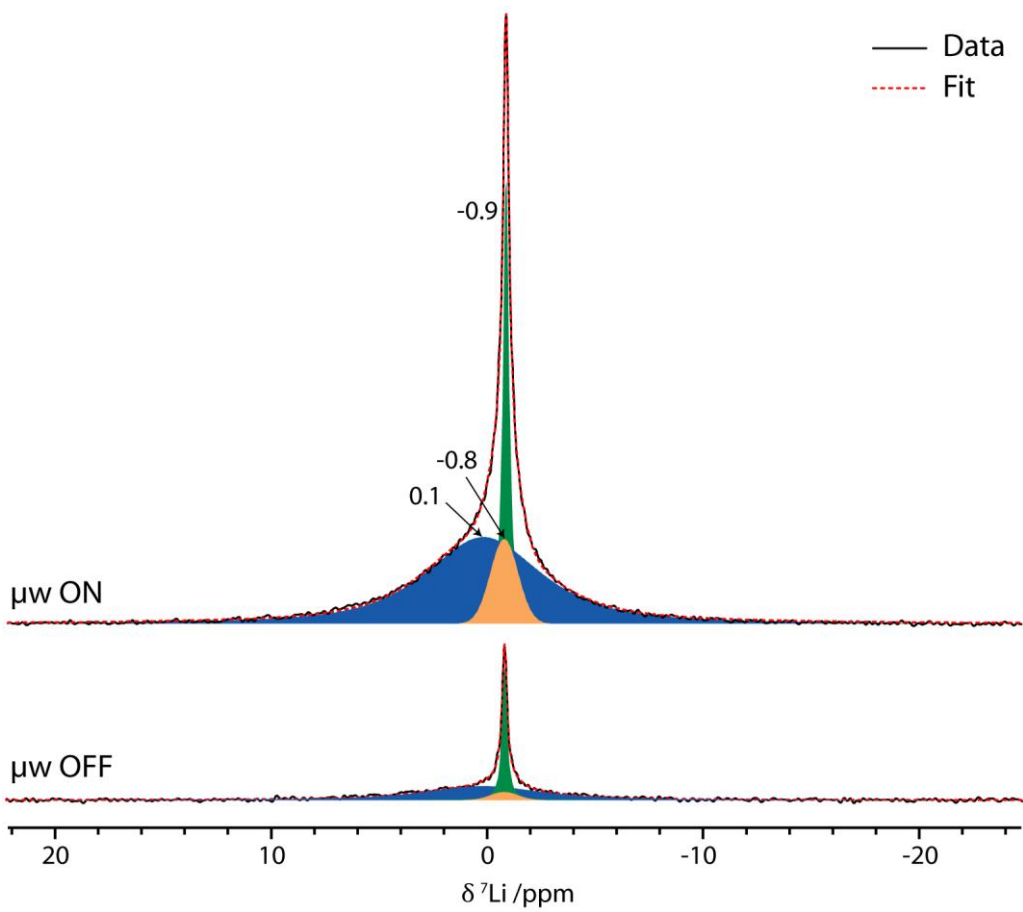


Figure S15: Deconvoluted ${}^7\text{Li}$ NMR spectra with and without microwave irradiation for microstructural lithium deposited with the FEC containing electrolyte (sample E, Figure 2d), recorded at room temperature, 14.1 T and 12.5 kHz MAS with a 1 s recycle delay and a Hahn echo pulse sequence.

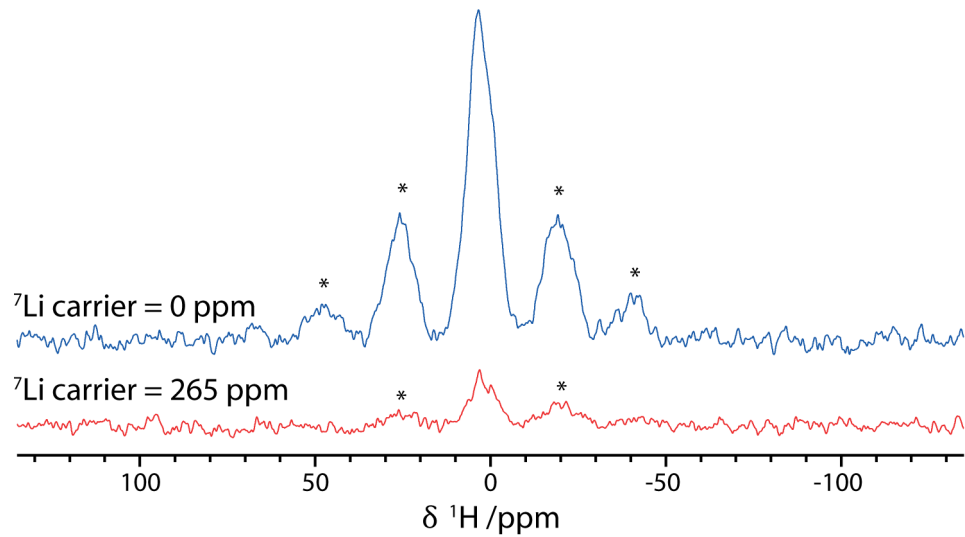


Figure S16: ${}^7\text{Li} \rightarrow {}^1\text{H}$ cross polarisation spectra for microstructural lithium produced with the LP30 electrolyte (sample D), with microwave irradiation and two different ${}^7\text{Li}$ carrier frequencies, recorded at 14.1 T and 12.5 kHz MAS using a 1 s recycle delay.

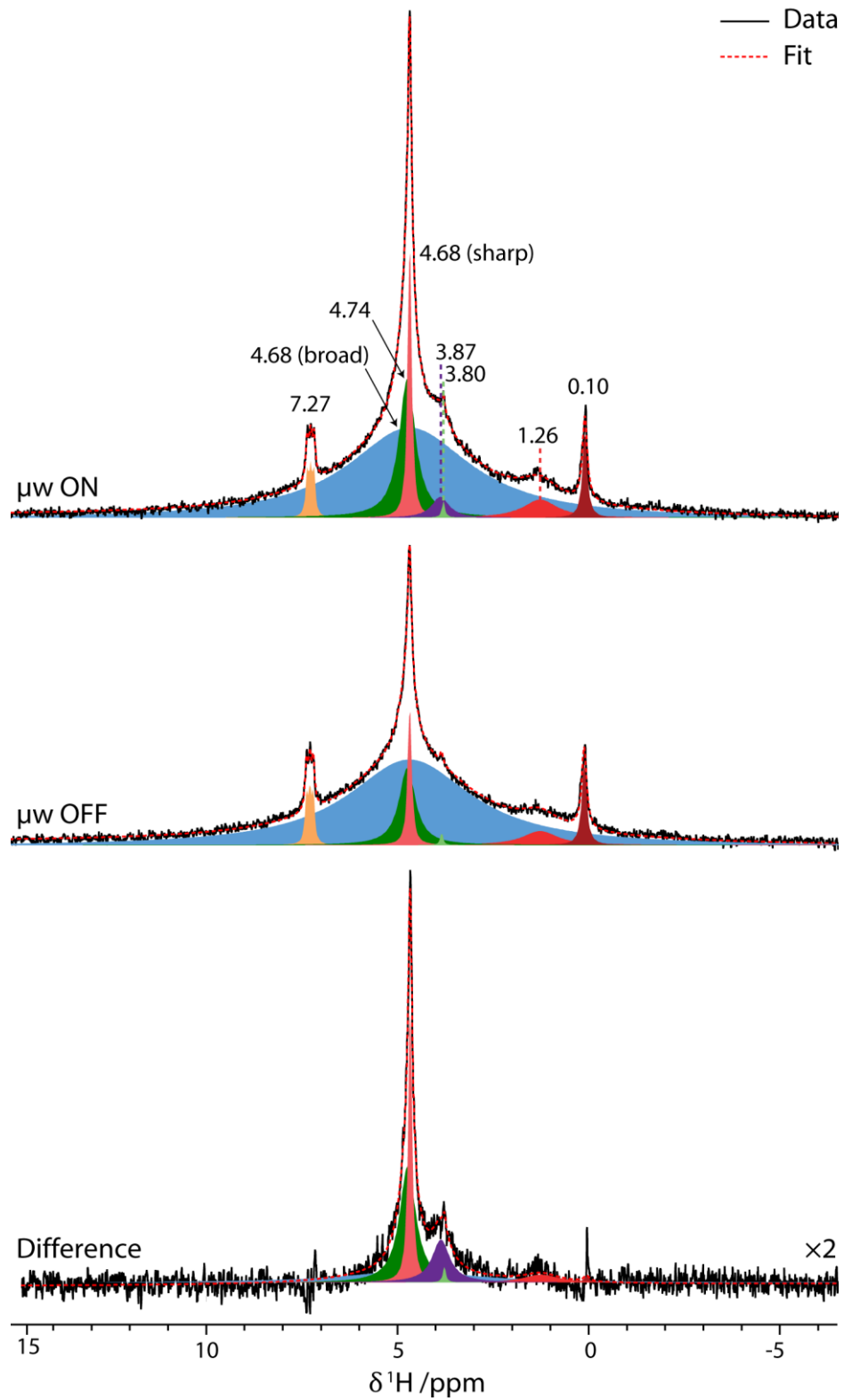


Figure S17: Deconvoluted ^1H NMR spectra with and without microwave irradiation and difference spectrum for microstructural lithium deposited with the LP30 electrolyte (sample D, Figure 2e), recorded at 240 K, 14.1 T and 12.5 kHz MAS with a 10 s recycle delay and a Hahn echo pulse sequence.

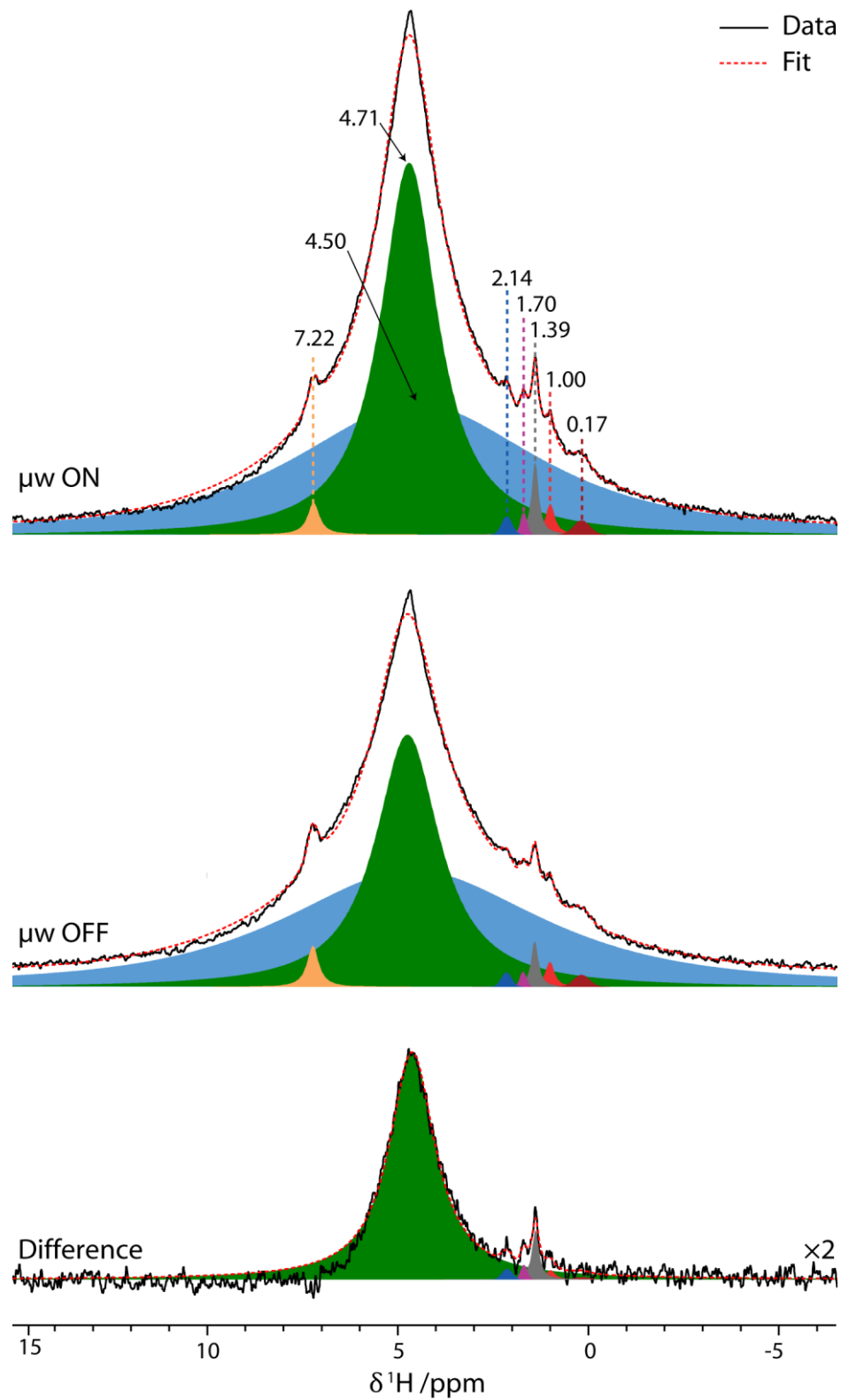


Figure S18: Deconvoluted ^1H NMR spectra with and without microwave irradiation and difference spectrum for microstructural lithium deposited with the LP30+FEC electrolyte (sample E, Figure 2g), recorded at 240 K, 14.1 T and 12.5 kHz MAS with a 10 s recycle delay and a Hahn echo pulse sequence.

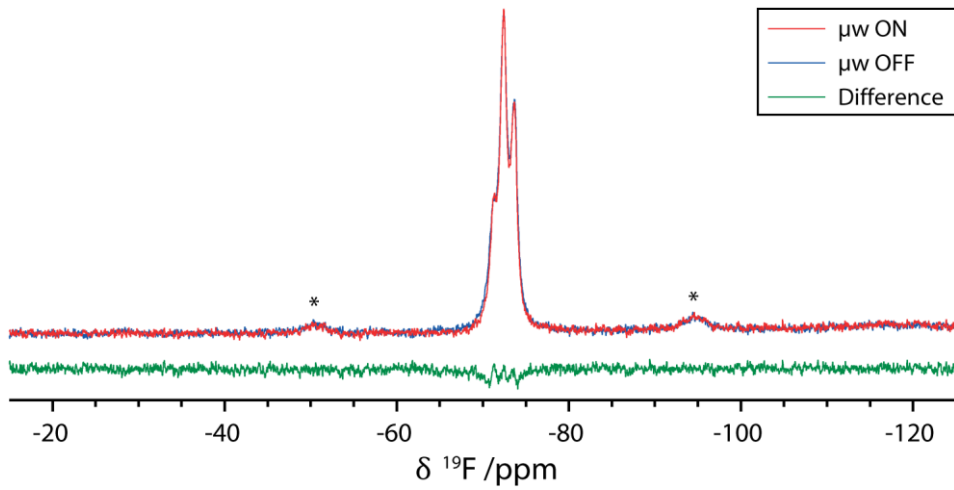


Figure S19: ^{19}F spectra of microstructural lithium produced with the LP30+FEC electrolyte (sample E), with and without microwave irradiation, recorded at 240 K, 14.1 T and 12.5 kHz MAS using a Hahn echo pulse sequence and a 30 s recycle delay.

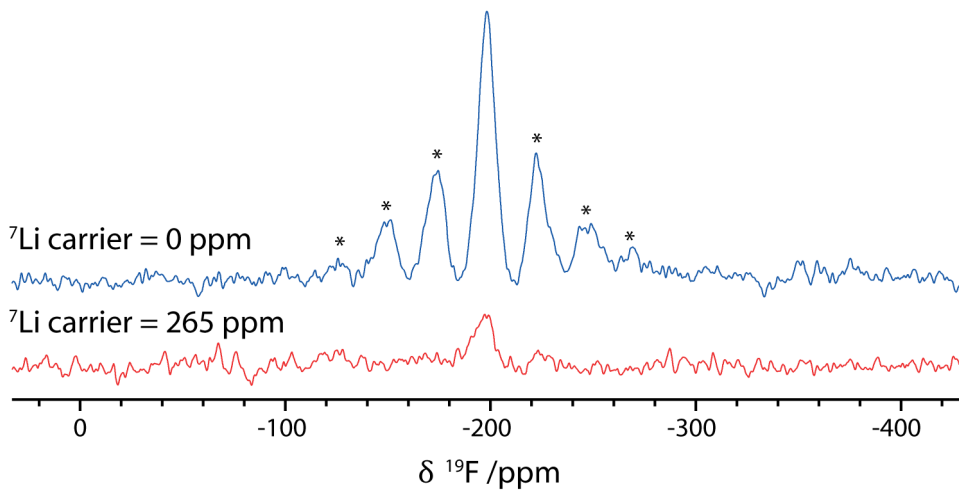


Figure S20: $^7\text{Li} \rightarrow ^{19}\text{F}$ cross polarisation spectra for microstructural lithium produced with the LP30+FEC electrolyte (sample E), with microwave irradiation and two different ^7Li carrier frequencies, recorded at 14.1 T and 12.5 kHz MAS using a 1 s recycle delay.

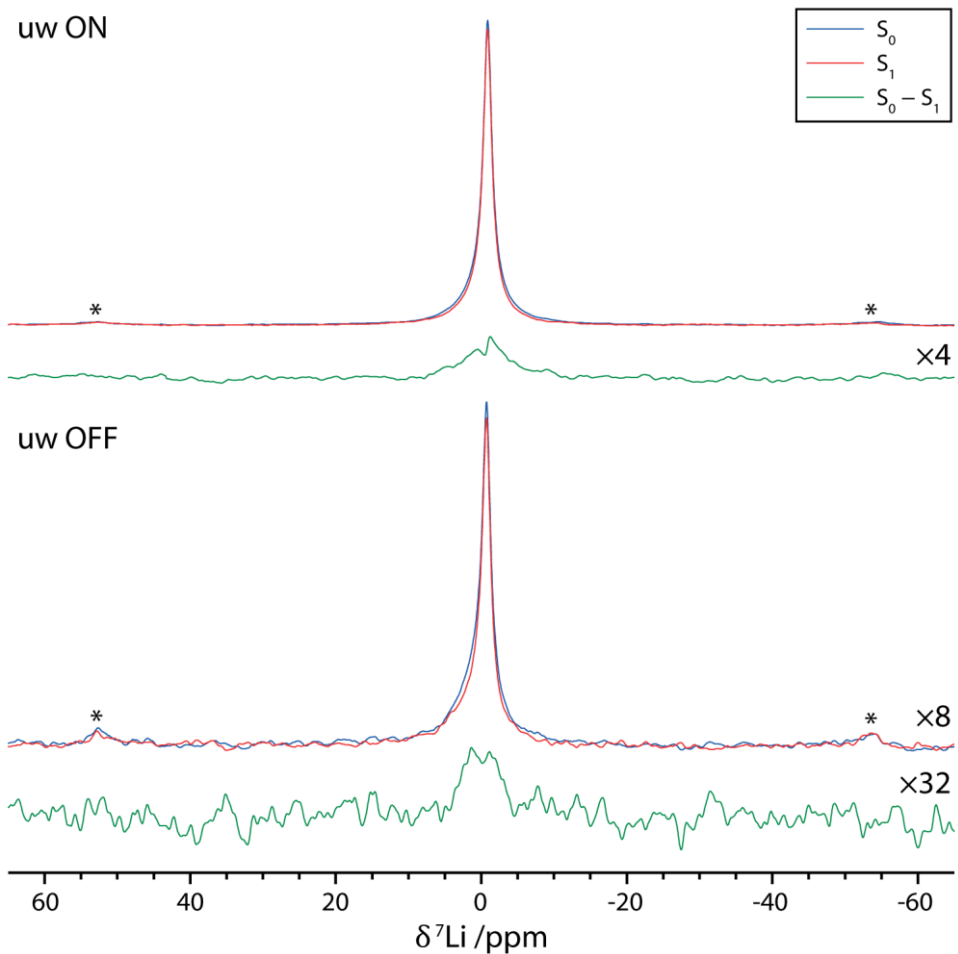


Figure S21: ${}^7\text{Li}\{{}^{19}\text{F}\}$ REDOR spectra with and without microwave irradiation of microstructural lithium produced with the LP30+FEC electrolyte (sample E), recorded at 14.1 T and 12.5 kHz MAS, using a 10 s recycle delay, with (S_1) and without (S_0) 5 rotor periods of recoupling, each recorded with 32 scans. Although the differences are minor, it can be seen that the dephasing is a real effect because if the ${}^{19}\text{F}$ carrier is moved by 1 MHz, the dephasing disappears (Figure S23).

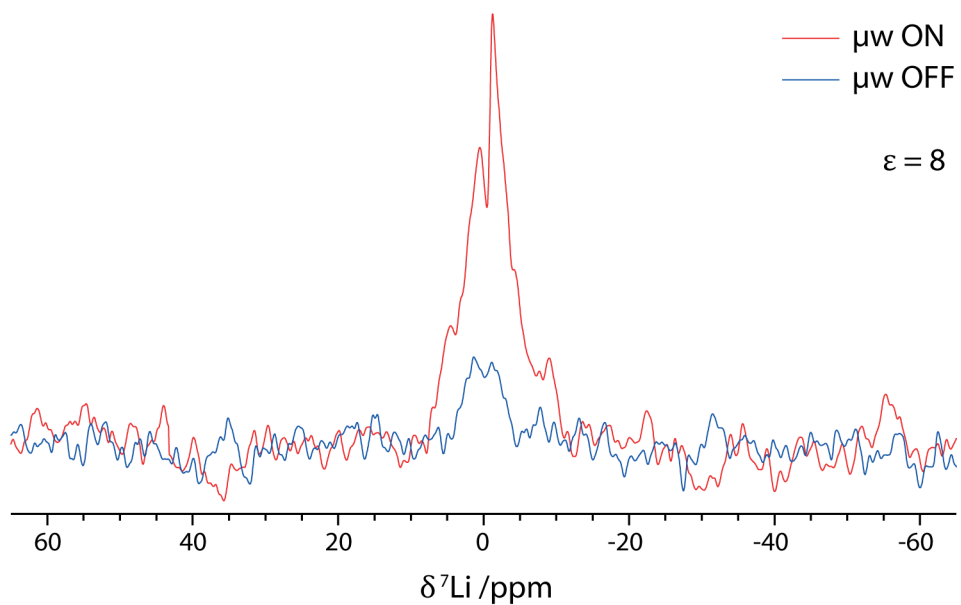


Figure S22: Direct comparison of the REDOR difference spectra for microstructural lithium produced with the LP30+FEC electrolyte (sample E), with and without microwave irradiation (see Figure S21).

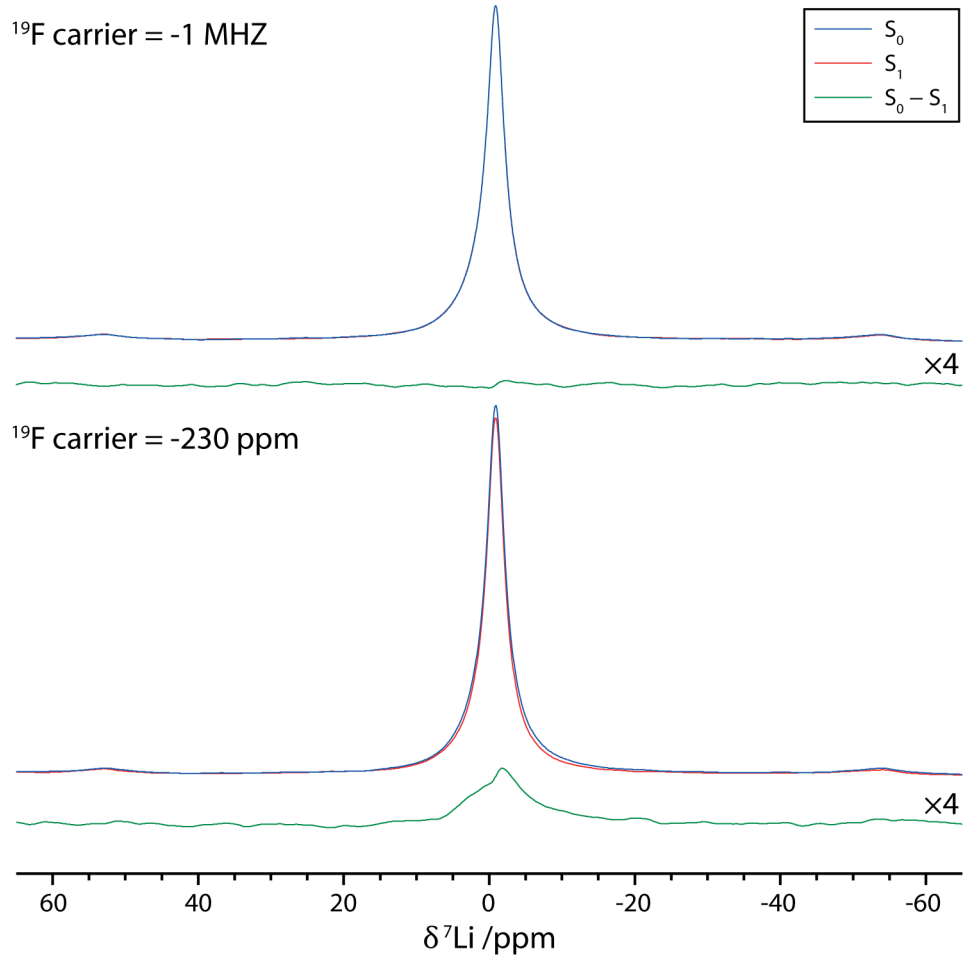


Figure S23: ${}^7\text{Li}\{{}^{19}\text{F}\}$ REDOR spectra of microstructural lithium produced with the LP30+FEC electrolyte (sample E) with microwave irradiation and two different ${}^{19}\text{F}$ carrier frequencies, recorded at 14.1 T and 12.5 kHz MAS, using a 1 s recycle delay, with (S_1) and without (S_0) 5 rotor periods of recoupling, each recorded with 160 scans.

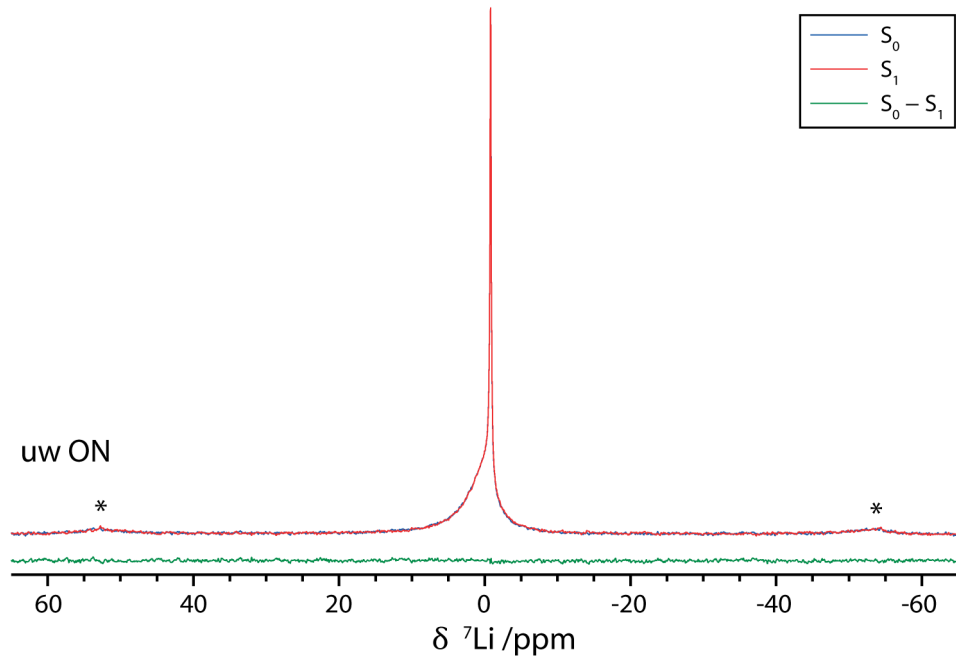


Figure S24: ${}^7\text{Li}\{{}^{19}\text{F}\}$ REDOR spectra of microstructural lithium produced with the LP30 electrolyte (sample D) with microwave irradiation, recorded at 14.1 T and 12.5 kHz MAS, using a 1 s recycle delay, with (S_1) and without (S_0) 5 rotor periods of recoupling, each recorded with 160 scans.

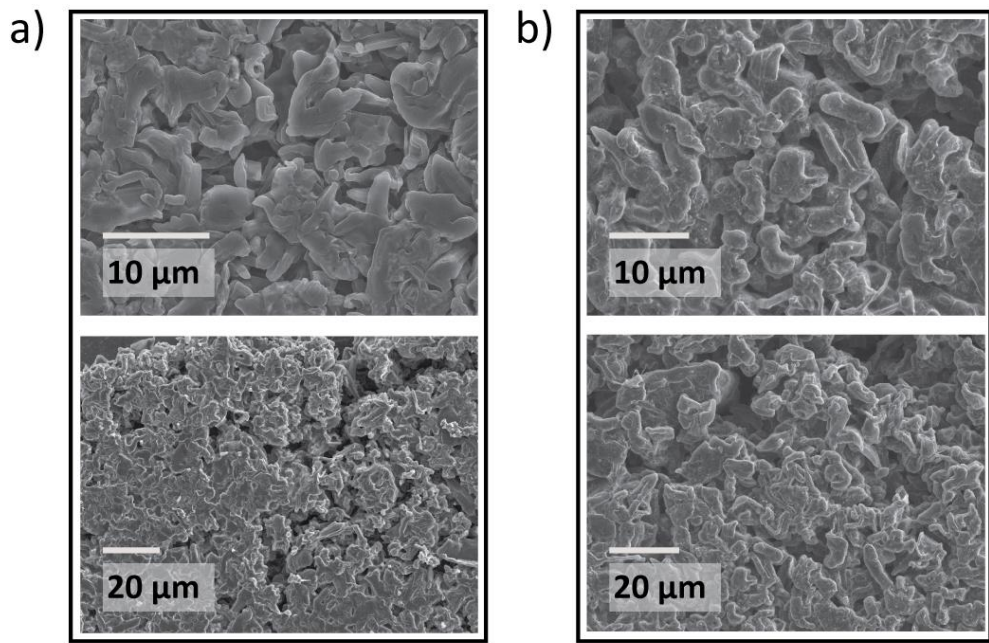


Figure S25: SEM images of lithium microstructures deposited on lithium metal disks using a current density of 1.25 mA cm^{-2} and either a) the LP30 electrolyte or b) the LP30+FEC electrolyte. The microstructures were not scraped off the disks.

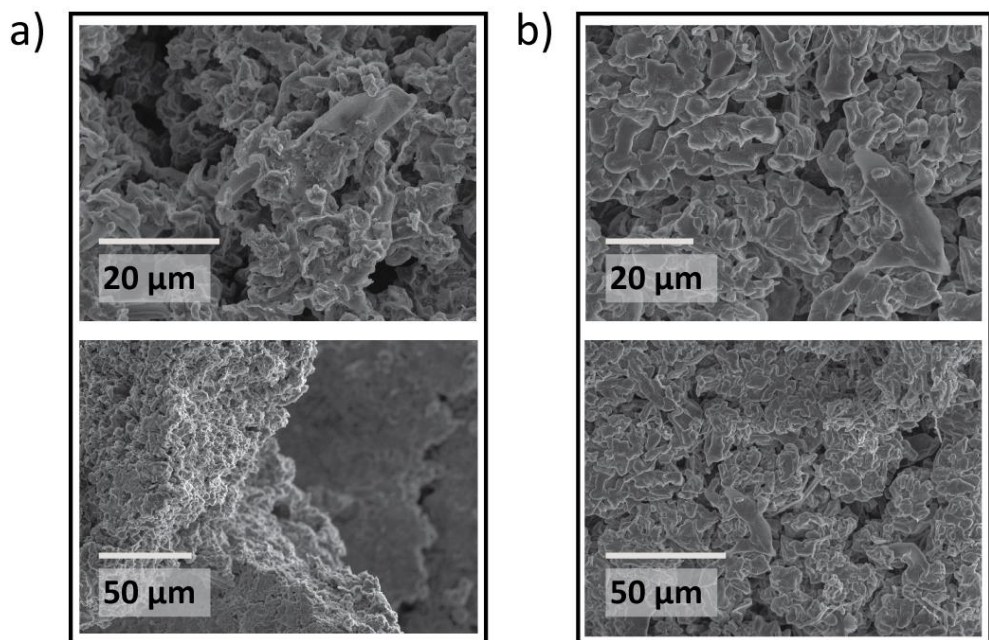


Figure S26: SEM images of lithium microstructures deposited on lithium metal disks using a current density of 1.25 mA cm^{-2} and either a) the LP30 electrolyte or b) the LP30+FEC electrolyte, after the microstructures had been scraped off the disks.